GPPS | JOURNAL

JOURNAL OF THE GLOBAL POWER AND PROPULSION SOCIETY
journal.gpps.global

Design guidelines for high-pressure ratio supersonic radial-inflow turbines of organic Rankine cycle systems

Original article

Article history:
Submission date: 6 February 2024
Final revision date: 29 August 2024
Acceptance date: 30 October 2024
Publication date: 11 April 2025

*Correspondence:
MP: m.pini@tudelft.nl

Peer review:
Single blind

Keywords:
ORC; design guidelines; supersonic RIT

Citation:
Majer M., Pini M. (2025). Design guidelines for high-pressure ratio supersonic radial-inflow turbines of organic Rankine cycle systems. Journal of the Global Power and Propulsion Society. 9: 19–46.
https://doi.org/10.33737/jgpps/195437

Matteo Majer[1], Matteo Pini[1,*]

[1]*Propulsion and Power, Faculty of Aerospace Engineering, Delft University of Technology, Kluyverweg 1, 2629 HS, Delft, The Netherlands*

Abstract

The radial-inflow turbine (RIT) is a widely adopted turbo-expander in power and propulsion systems of low-to-medium power capacity due to its high efficiency and compactness. Compared to conventional radial turbines for gas turbines and air cycle machines, the design of expanders for high-temperature organic Rankine cycle power systems involves additional challenges, as these machines operate with very high expansion or volumetric flow ratio and partly or entirely in the nonideal compressible fluid dynamic regime. This study examines the impact of the working fluid, of the volumetric flow ratio, and of the nonideal thermodynamic effects on the design guidelines for RIT. To this purpose, a reduced-order modeling framework for turbine fluid-dynamic design encompassing a loss model based on first principles is developed and verified against results from uRANS. Results highlighted that at the geometrical scale of interest the impact of the working fluid molecular complexity on the efficiency is marginal. Moreover, it is shown that the average isentropic pressure-volume exponent ($\bar{\gamma}_{Pv}$) can be used to predict the magnitude of nonideal thermodynamic effects on the stage efficiency, whose variation depends on the value of the volumetric flow ratio and of the work and flow coefficients. Design guidelines that can be used for preliminary turbine design in system-level calculations are presented in graphical form, and illustrate the relation between the optimal set of stage duty coefficients, i.e., the work and flow coefficients that maximize the efficiency, the stage efficiency, the volumetric flow ratio, and the similarity parameter $\bar{\gamma}_{Pv}$.

Introduction

Future propulsion and power systems will arguably benefit from adopting highly efficient and lightweight radial-inflow turbines (RITs) (Bahamonde et al., 2017). Examples of such systems include cryogenic rocket engines (Nosaka et al., 2004; Mack et al., 2006; Leto and Bonfiglioli, 2017), organic Rankine cycle (ORC) turbogenerators for waste heat to power from prime engines (Najjar and Radhwan, 1988; Krempus et al., 2023), air supply systems for fuel cells-based propulsion (Wittmann et al., 2021a,b, 2022), as well as heat pumps and cryo-coolers based on the reversed Brayton cycle (Swift et al., 1999; Dhillon and Ghosh, 2021). Other relevant applications of RITs are in stationary and mobile hydrogen storage systems for energy recovery (Symes et al., 2021). RITs for all these novel systems can feature pressure ratios substantially higher than those commonly found in radial turbines employed in turbochargers and small gas turbines (GT) for auxiliary power units (APU) (Rodgers, 1987; Jones, 1996).

From a fluid dynamic perspective, the most unconventional RITs are arguably those of high-temperature ORC turbogenerators (*hiTORC-RIT*), as they are characterized by ultra-high pressure or volumetric flow ratio (above 30) leading to supersonic flows, and by the occurrence of nonideal thermodynamic effects in the stator (Tosto, 2023). These attributes are a well-known consequence of the use of high molecular complexity (HMC) fluids (Guardone et al., 2024) in such systems, like siloxanes and hydrocarbons (Colonna et al., 2015). Recent works (De Servi et al., 2019; Cappiello and Tuccillo, 2021a,b) that investigated the fluid dynamic performance of ≈10 kW power capacity *hiTORC-RIT* operating with siloxane MM revealed that, despite the high Mach numbers of the flow downstream of the stator (order of 2), these turbines can feature total-total efficiency in excess of 80%, due to the possibility of selecting values of the design work coefficient in the same range suggested by literature (i.e., 0.6–1.3). Stator-impeller interaction effects due to shocks and expansion waves can however greatly affect the efficiency and the operation of these machines (Cappiello and Tuccillo, 2021a; Cappiello et al., 2022). Nonideal thermodynamic effects, like non-monotone variations of the Mach number of the flow through the stator and peculiar flow phenomena ascribed to the fluid molecular complexity as the incompressible-like behavior of the boundary layer, influence the loss mechanisms (Tosto et al., 2024) and the design layout of the stage (Giuffre' and Pini, 2021).

The seminal work on design guidelines for RITs of ORC systems was carried out by Perdichizzi and Lozza (1987), who investigated the fluid dynamic performance of stages operating at low and medium volumetric flow ratio VR, up to $VR = 10$. The stator losses were predicted using the Craig and Cox correlation for axial turbines, adapted to radial vanes, while the impeller passage loss was computed using the models proposed by Glassman, (1976), including viscous drag on the blade profile and secondary flow loss due to tip leakage. The numerical results were found in good agreement with experimental data available for radial turbines. Two important findings were derived from the study: first, the volumetric flow ratio allows comparing the fluid dynamic performance of stages operating with different working fluids and expansion ratios PR using a single dimensionless parameter, $VR = PR^{1/\gamma}$, with γ the ideal gas specific heat ratio. Second, regardless the volumetric flow ratio, the maximum efficiency value is obtained for a value of the specific speed $N_s \simeq 0.1$, suggesting that the optimal value of the stage duty coefficients is not affected by VR. The more recent work of Mounier et al. (2018) documenting design guidelines for RITs of low-to-medium temperature ORC systems reported plots of the turbine efficiency as a function of N_s and the specific diameter D_s. The study highlighted that the efficiency value becomes dependent on N_s and D_s as the pressure ratio PR exceeds 10. In addition, the optimal D_s value decreases appreciably as compressibility effects become more significant. The sensitivity of the calculated stage efficiency to the fluid molecular complexity was assessed on a limited range of working fluids, considering refrigerants of increasing molecular complexity. Results showed negligible efficiency variations by varying the working fluid, corroborating that PR is an appropriate similarity parameter when comparing the fluid dynamic performance of turbines operating with fluids of similar molecular complexity, i.e., of the same class. In analogy to the study of Perdichizzi and Lozza (1987), losses were modeled according to empirical correlations and contribution of the shock waves to losses was not accounted for. Manfredi et al. (2021) developed a mean-line design model for *hiTORC-RIT*, validating it against experimental data available for radial-inflow turbines operating at both on- and off-design conditions. A semi-empirical loss model was used to predict the turbine efficiency. Notably, the models of Glassman (1976) and Baines (1998) were adopted to compute the stator and impeller passage losses, while mixing losses were computed using first principles and a control volume approach, as recommended in (De Servi et al., 2019; Giuffre' and Pini, 2021; Tosto et al., 2022). The stator-impeller radial gap and the disk windage friction losses were estimated using the methods reported in Whitfield and Baines (1990). In a subsequent study, Manfredi et al. (2023) concluded that the optimal choice of VR and of the size parameter SP is not dictated by the working fluid. Considering a wide range of fluid classes, from refrigerants through hydrocarbons to siloxanes, the authors found a deviation of about 0.5% in the optimal efficiency of stages designed for different working fluids.

Notwithstanding the recent works, a conclusive study presenting best design practices for *hiTORC-RIT* and clarifying the role of the fluid molecular complexity and of nonideal thermodynamic effects to loss and efficiency is not available. Such knowledge gap is filled in this study, in which design guidelines formulated in accordance to a suited scaling analysis are documented. To this purpose, a reduced-order model (ROM) for turbine preliminary design was developed and verified against results obtained with unsteady RANS (uRANS) simulations. The ROM implements semi-empirical loss correlations adapted to nonideal flows and loss models for shock and mixing losses based on first principles. Results obtained with the ROM and corroborated via CFD simulations elucidate the impact of the volumetric flow ratio, of the working fluid, and that of nonideal thermodynamic effects on turbine efficiency and on the selection of duty coefficients for optimal stage design.

Theoretical framework

Generalized scaling law for radial-inflow turbines

The fluid dynamic efficiency of a radial turbine stage operating with a fluid in the ideal gas state can be expressed as

$$\eta = f(\psi, \phi, \mu, \alpha_{\text{out}}, \text{PR}, \gamma, \text{Re}, \boldsymbol{\sigma}), \tag{1}$$

where $\boldsymbol{\sigma}$ is the vector of the variables describing the geometrical characteristics of the stage, for instance the solidity or the trailing-edge to pitch ratio of both the stator and the impeller, and γ is the specific heat ratio of the fluid in the limit of dilute, i.e., perfect, gas. Equation 1 differs from that used to describe the fluid dynamic performance of axial turbomachine stages reported by, e.g., Giuffre' and Pini (2021), as for radial stages it is common practice to fix the absolute flow angle α_{out} at the outlet of the impeller rather than the degree of reaction. Moreover, since in radial stages the meridional flow velocity across the impeller is usually non constant, the ratio of meridional flow velocities $\mu = V_{m3}/V_{m2}$ appears as an additional independent variable in Equation 1. According to Giuffre' and Pini (2021), the impact of the fluid and its thermodynamic conditions on the stage fluid dynamic performance is primarily dependent on two quantities: the density or volumetric flow ratio VR, which replaces the pressure ratio PR in Equation 1, and the isentropic pressure-volume exponent, γ_{Pv}, which is the exponent that generalizes the isentropic ideal gas relation Pv^{γ} for nonideal thermodynamic states and that provides the magnitude of nonideal compressible fluid dynamic (NICFD) effects (Kouremenos and Kakatsios, 1985; Guardone et al., 2024). In the nonideal thermodynamic region, the value of γ_{Pv} depends on the fluid thermodynamic state, therefore an averaged value is needed to relate the effect of γ_{Pv} on the fluid dynamic performance of the stage. An average suited for expansion and compression processes in turbomachines is given by the following logarithmic relation

$$\bar{\gamma}_{Pv} = \frac{\ln P_1/P_2}{\ln v_2/v_1}, \tag{2}$$

where P and v are the pressure and specific-volume at the beginning (1) and at the end (2) of the expansion process, and $\bar{\gamma}_{Pv}$ is the exponent which satisfies $Pv^{\bar{\gamma}_{Pv}} = K$. The density ratio can then be approximated as $VR = PR^{(1/\bar{\gamma}_{Pv})}$. Both VR and $\bar{\gamma}_{Pv}$ are the parameters characterizing the fluid-dynamic performance of turbomachinery operating with the working fluid in thermodynamic states along the process partly or fully nonideal. Equation 1 can be consequently formulated as

$$\eta = f(\psi, \phi, \mu, \alpha_{\text{out}}, VR, \bar{\gamma}_{Pv}, \text{Re}, \boldsymbol{\sigma}). \tag{3}$$

Equation 3 is referred to as the generalized scaling law for design of radial-inflow turbines.

NICFD effects on losses in turbines

While the effect of γ on the loss mechanisms and turbine stage efficiency has been adequately investigated (Baumgärtner et al., 2020a,b; Giuffre' and Pini, 2021; Tosto et al., 2022), studies documenting the influence of $\bar{\gamma}_{Pv}$ on losses are limited. Giuffre' and Pini (2021) found that, for VR values in the range of 3–5, axial turbine stages operating with working fluids in thermodynamic states for which $\bar{\gamma}_{Pv} > \gamma$ along the process are characterized by comparatively higher losses due to enhanced compressibility effects. On the contrary, lower losses characterize stages operating with complex fluid molecules in ideal gas conditions, for which $\bar{\gamma}_{Pv} = \gamma \to 1$. However, the magnitude of NICFD effects on losses remains dependent on the fluid and its thermodynamic states along the expansion process. Using a simple analytical model, Denton (1993) demonstrated that the entropy generation across normal shock waves scales reasonably well with γ. By replacing γ with $\bar{\gamma}_{Pv}$, the model can be generalized to nonideal compressible flows. The equation to compute the efficiency decrease occurring across a normal shock reads

$$\Delta\eta \approx \frac{\bar{\gamma}_{Pv} + 1}{12\bar{\gamma}_{Pv}^2}\left(VR_{sh}^{\bar{\gamma}_{Pv}} - 1\right)^2, \tag{4}$$

and shows that for a fixed VR_{sh} across the shock, the efficiency deficit is proportional to $\bar{\gamma}_{Pv}$, as shown in the left-hand side plot of Figure 1.

Recent investigations on flows of fluids of varying molecular complexity in transonic and supersonic blade rows (Baumgärtner et al., 2020a) highlighted that the wake mixing process and the associated loss are largely affected by the γ value downstream of the trailing edge. If $\bar{\gamma}_{Pv}$ is introduced in place of γ, the relation can be extended to nonideal compressible flows and written in the form

$$\frac{\zeta_{\mathrm{mo}}}{\zeta_{\mathrm{mo}}^{\mathrm{Air}}} = a(\bar{\gamma}_{Pv}) \cdot (\mathrm{M}_{\mathrm{out}} + 0.25) + 1, \tag{5}$$

in which $\mathrm{M}_{\mathrm{out}}$ is the Mach number downstream of the cascade. The value of $a(\bar{\gamma}_{Pv})$ was computed by fitting of the data obtained from two-dimensional CFD simulations performed on turbine cascades operating with working fluids in ideal gas conditions, and with $\gamma \in (1.08, 1.67)$, yielding

$$a(\bar{\gamma}_{Pv}) = 0.1014\bar{\gamma}_{Pv}^3 - 0.2728\bar{\gamma}_{Pv}^2 - 0.122\bar{\gamma}_{Pv} + 0.4272.$$

The right plot of Figure 1 shows the trend of the mixing losses as a function of the average isentropic pressure volume exponent. Higher efficiency penalties due to wake-mixing occur in mixing processes of fluids made by complex molecules and in thermodynamic states of the fluid for which $\bar{\gamma}_{Pv} < \gamma$. Moreover, the higher the Mach number downstream of the cascade, the higher the loss for complex fluids in the nonideal thermodynamic regime.

The results shown thus far point out that any loss correlation developed for ideal gas flows should be adapted to compute losses and efficiency trends of radial turbines operating with working fluids in nonideal thermodynamic states by, at least, introducing suitable values of $\bar{\gamma}_{Pv}$ into the model.

Turbine design methodology

The turbomachinery design program *TurboSim* developed in this work is a reduced-order model (ROM) based on a quasi-3D calculation method of the flow passing through a radial-inflow turbine stage, composed by a stator and an impeller. The flow quantities and the main machine dimensions are evaluated at four sections in the stream-wise direction along the flow path, i.e., at the inlet and outlet of each blade row, as depicted in Figure 2. However, as opposed to a conventional lumped parameters approach, the flow quantities at each section are also calculated at an arbitrary number of locations along the span, to take three-dimensional effects into account. The most relevant 3D flow distribution, e.g. free- or controlled-vortex, can be imposed at the

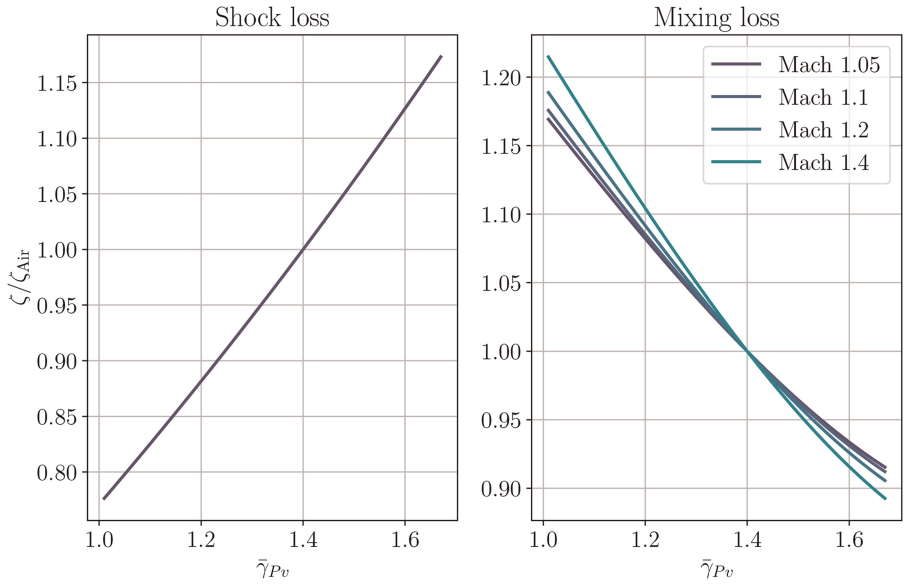

Figure 1. Shock loss (left) and mixing loss at increasing cascade downstream Mach number (right) as a function of the generalized isentropic pressure-volume exponent $\bar{\gamma}_{Pv}$. The loss coefficients are normalized by the one of air in ideal gas conditions ($\bar{\gamma}_{Pv} = 1.4$). Loss is computed assuming $VR_{sh} = 1.2$.

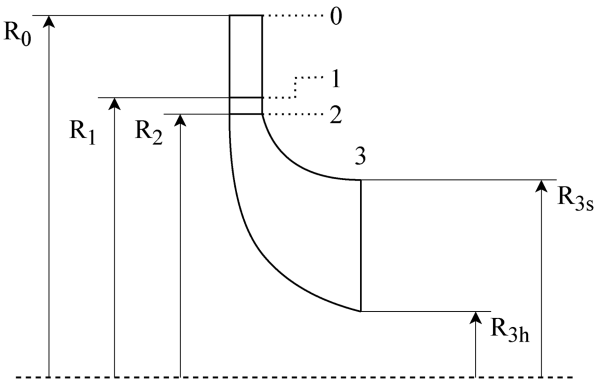

Figure 2. Meridional view of a radial-inflow turbine stage with all the relevant dimensions indicated.

impeller outlet section to optimize the stage performance. The numerical framework is programmed in Python, and coupled to the thermodynamic libraries of the REFPROP software (Huber et al., 2022).

A simplified workflow illustrating the design methodology implemented in *TurboSim* is shown in Figure 3. The design is performed in two main steps, highlighted in the figure by means of the colored boxes. With reference to the yellow box, the stage is first sized by assuming isentropic and uniform flow along the span; the actual flow quantities at each span-wise location are subsequently calculated by selecting a span-wise flow distribution and by applying a loss model (red box). The whole design process is iterative, with several internal loops highlighted in the figure by the arrow wrapping around each block of the diagram. Convergence is achieved when the calculated mass-flow averaged pressure ratio $\overline{PR}$ equals the user specified value. In the following, the calculation process of the isentropic flow quantities along the machine and the method for loss accounting is described in more detail. Moreover, additional information on the algorithm used to achieve convergence of the exducer radius ratio R_{3h}/R_{3s} have been provided in Appendix B.

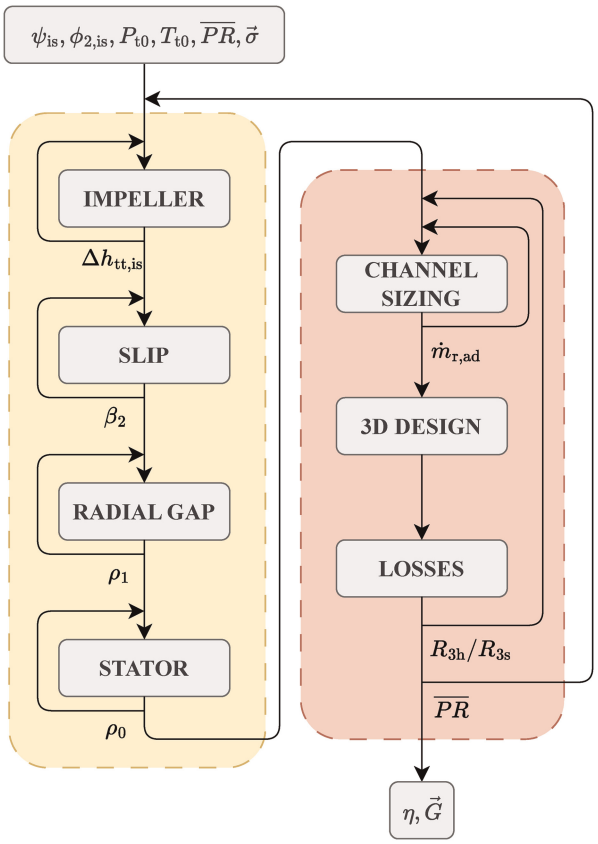

Figure 3. Workflow diagram of the turbine preliminary design method.

Impeller

The impeller is sized according to the classical method based on the work and flow coefficients (Chen and Baines, 1994). Given ψ_{is} and $\phi_{2,is}$ and the stage boundary conditions T_{t0}, P_{t0}, $\overline{PR}(VR, \bar{\gamma}_{Pv})$, the inlet and outlet velocity triangles at mid span-wise section are computed. The tip peripheral velocity is calculated as

$$U_2 = \sqrt{\frac{\Delta h_{tt,is}}{\psi_{is}}}, \tag{6}$$

where the isentropic enthalpy drop $\Delta h_{tt,is}$ is defined by the stage boundary conditions. The inlet meridional velocity can be calculated from the flow coefficient $\phi_{2,is}$ and U_2 as

$$V_{m2,is} = \phi_{2,is} \cdot U_2. \tag{7}$$

Using the impeller design variables ν, μ and α_3, the outlet velocity triangle is retrieved, and so the outlet work coefficient $\psi_{3,is} = V_{\theta 3,is}/U_3$. The inlet work coefficient $\psi_{2,is}$ is determined by means of the adimensional Euler equation for isentropic flow:

$$\psi_{is} = \psi_{2,is} - \nu \cdot \psi_{3,is}, \tag{8}$$

$$\psi_{2,is} = \psi_{is} + \nu \cdot \psi_{3,is}. \tag{9}$$

Rearranging Equation 8 into Equation 9 yields the value of $\psi_{2,is}$, from which $V_{\theta 2,is}$ can be finally computed. The above described procedure is straightforward if the total-total pressure or density ratio are specified, because $\Delta h_{tt,is}$ in Equation 6 is directly calculated. If the total-static pressure or density ratio are instead specified, the calculation of $\Delta h_{tt,is}$ needed in Equation 6 becomes iterative, using the total-static isentropic enthalpy drop $\Delta h_{ts,is}$ as first guess to compute U_2.

The prediction of the optimal impeller incidence angle is based on the method proposed by Chen and Baines (1994). The impeller blade count is computed according to an empirical model (Glassman, 1976), see Equation 10, rigorously valid only for radial bladed impellers.

$$N = \frac{\pi}{30^\circ}(110^\circ - \alpha_{2,is})\tan(\alpha_{2,is}). \tag{10}$$

Given the blade count N and the isentropic tangential velocity $V_{\theta 2,is}$, Equation 11 allows one to compute the slip factor σ as

$$\sigma = 1 - \frac{0.63\pi}{N}\sin(\xi)\cos(\beta_{2g}). \tag{11}$$

In Equation 11, ξ is referred to as the inlet cone angle, namely the angle between the meridional direction and the rotation axis in the meridional plane at the inlet of the impeller. β_{2g} is the blade metal angle at the impeller inlet, initially assumed to be equal to the value of the relative flow angle $\beta_{2,is}$. The slip velocity difference ΔV_θ^*, is defined as in Equation 12 and is used to compute the optimal impeller inlet velocity triangle.

$$\Delta V_\theta^* = V_{\theta 2,is} \cdot \left(\frac{1}{\sigma} - 1\right). \tag{12}$$

Given that the blade count N is a function of the impeller inlet absolute flow angle $\alpha_{2,is}$, the slip angle is calculated by iteratively solving Equations 10–12. The absolute flow tangential velocity is finally given by

$$V'_{\theta 2} = V_{\theta 2} - \Delta V_\theta^*. \tag{13}$$

Note that, as opposed to common design practices for radial-inflow turbines, the design methodology described here can lead to impellers characterized by non-zero blade sweep angles at the inlet. As impellers of supersonic ORC radial turbines operate at temperatures not exceeding 250–300 °C and feature relatively low peripheral speed, thus comparatively low thermo-mechanical stresses, sweep angles up to 45° can be adopted.

Radial gap

The flow quantities at the outlet of the stator vane are determined by assuming that the flow distribution follows a free vortex law in the radial gap. Two further design variables, namely the radial gap span ratio b_2/b_1 and the radial gap radius ratio R_2/R_1 are specified. The conservation of mass, angular momentum and energy (Equations 14–16) between section 1 and 2 of Figure 2 are written as

$$\frac{V_{m1}}{V_{m2}} = \frac{\rho_2}{\rho_1}\frac{R_2}{R_1}\frac{b_2}{b_1}, \tag{14}$$

$$\frac{V_{\theta 1}}{V_{\theta 2}} = \frac{R_2}{R_1}, \tag{15}$$

$$h_1 = h_{t1} - \frac{V_1^2}{2}. \tag{16}$$

The system of non-linear equations is solved by iterating on the density ρ_1.

Radial stator

The flow quantities at the inlet of the radial vane are calculated by specifying the value of the absolute inlet flow angle α_0, the radius ratio R_1/R_0, and the vane span ratio b_1/b_0. The continuity equation

$$V_{m0} = V_{m1}\frac{\rho_1}{\rho_0}\frac{R_1}{R_0}\frac{b_1}{b_0}, \tag{17}$$

and the energy balance

$$h_0 = h_{t0} - \frac{V_0^2}{2}, \tag{18}$$

are iteratively solved to find the inlet flow velocity and the fluid thermodynamic properties.

Calculation of turbine efficiency

The total-total turbine efficiency is computed according to

$$\eta_{tt} = 1 - T_{1,is} \cdot \sum \Delta s_{st} - T_{3,is} \cdot \sum \Delta s_{\text{imp}}, \tag{19}$$

where the term $T_{is} \cdot \sum \Delta s$ is the overall efficiency penalty of the blade row due to the various loss mechanisms. The modeling of losses is documented in the following.

Loss accounting

Stator passage loss

As radial vanes of supersonic RITs are typically constituted by prismatic blades featuring converging-diverging nozzle profiles, secondary flow losses are often negligible with respect to boundary layer losses occurring on the blades and on the endwalls. The model of Meitner and Glassman (1983) based on the two-dimensional boundary layer theory was adopted for the computation of blade profile losses

$$\zeta_{2D} = \frac{E(Q) \cdot (\theta/g)}{\cos\alpha_1 - (t/g) - H(Q) \cdot (\theta/g)}, \tag{20}$$

as also recommended in Manfredi et al. (2021).

In Equation 20, E is the energy factor and H the shape factor of the boundary layer, calculated as suggested by Meitner and Glassman (1983). The angle α_1 is the stator outlet flow angle. The quantities θ and t are the momentum thickness of the boundary layer and the blade thickness at the trailing edge, normalized by the pitch g.

The calculation of the boundary layer factors E and H requires the determination of

$$Q = \frac{\bar{\gamma}_{Pv} - 1}{\bar{\gamma}_{Pv} + 1} \cdot \left(\frac{V_1}{V_{cr}}\right)^2, \tag{21}$$

that depends on the outlet flow conditions, where V_1 is the stator outlet flow velocity and V_{cr} is the critical velocity corresponding to a chocked flow. Since in Equation 21 $\bar{\gamma}_{Pv}$ corresponds to the average value between sections 0 and 1, the calculation of the loss coefficient becomes iterative. The entropy change due to profile loss is therefore obtained from

$$\Delta s_{st,\text{prof}} = s(h_1, P_1) - s_0, \tag{22}$$

where $h_1 = h_{t0} - V_{1,is} \cdot \sqrt{1 - \zeta_{2D}}$.

Following Denton (1993), the entropy generation due to endwall loss is obtained by numerical integration of the right hand side term of

$$\Delta s_{st,ew} = 2C_D \cdot \frac{\int_{A_{ew}} \rho V^3 / T dA}{\dot{m}}. \tag{23}$$

In the equation, ρ, V and T are the free stream flow quantities at the edge of the boundary layer, while the values of the dissipation coefficient C_D is assumed to be constant (Denton, 1993) and was listed in Appendix C. For simplicity, a rectangular velocity distribution (Denton, 1993) was assumed to compute the freestream quantities within the bladed channel. Coull (2017) compared losses obtained with such a simple distribution against those obtained with a velocity distribution computed with CFD, and found small difference in the loss coefficient.

Mixing loss

Losses generated by wake mixing downstream of stator vanes and impeller blades are computed using the method documented in Denton (1993), in which the effective base pressure coefficient is computed as

$$C_{P_\text{b},\text{eff}} = \left(\frac{P_\text{b}}{P_\text{ref}} - 1\right) \cdot \frac{2}{\gamma_{Pv}\, \text{M}_\text{ref}^2} \cdot \frac{t}{g}. \tag{24}$$

Equation 24 is a generalization of the base pressure coefficient model to compressible flows and arbitrary working fluids (Baumgärtner et al., 2020a). In the equation, P_ref and M_ref are the reference pressure and Mach number, namely the total pressure at the inlet and the isentropic Mach number at the outlet of the cascade, while P_b is the base pressure, whose value is a function of the cascade total-static pressure ratio and of the critical area ratio, based on cascade experimental data (Sieverding et al., 1980). The entropy change associated to wake mixing losses is eventually expressed as

$$\Delta s_{mx} = \left(-\frac{C_{P_b,\text{eff}} \cdot t}{g} + \frac{2\theta}{g} - \left(\frac{\delta^* + t}{g}\right)^2\right) \cdot \frac{V_{\text{out},is}^2}{2T_{\text{out},is}}, \tag{25}$$

in which θ and δ^* are the momentum and the displacement thickness of the boundary layer at the trailing edge, calculated considering the scaling parameters in Appendix C which are valid for both the stator vanes and the impeller blades. g is the cascade pitch and t the trailing edge thickness.

Shock loss

The entropy generation across shock waves formed at the trailing edge of either stator vanes and impeller blades is computed using the model based on first-principles documented in (Vimercati et al., 2018) and (Giuffre' and Pini, 2021). The governing equations are the Rankine-Hugoniot (RH) relations for an oblique shock, reported

by Equation 26–29.

$$h_B - h_A = \frac{1}{2}(P_B - P_A)(\nu_B - \nu_A) \tag{26}$$

$$-\frac{P_B - P_A}{\nu_B - \nu_A} = (\rho_A V_A \sin\varepsilon)^2 \tag{27}$$

$$\rho_A \tan\varepsilon = \rho_B \tan\varepsilon - \delta \tag{28}$$

$$V_A \cos\varepsilon = V_B \cos\varepsilon - \delta, \tag{29}$$

where ε is the shock angle and δ is the flow deviation past the shock. The flow state upstream of the shock is denoted by A, while state B identifies the downstream conditions. The shock angle depends on the upstream flow conditions through the following relation taken from AMES (1953), only valid for weak shock waves where the normal component of the upstream Mach number $M_A \cdot \sin\varepsilon$ is slightly larger than 1

$$\varepsilon = \arcsin\left(\frac{1}{M_A}\right) + \frac{\Gamma_A}{2}\frac{M_A^2}{M_A^2 - 1}\cdot\delta + \mathcal{O}(\delta^2). \tag{30}$$

The entropy change across the shock is equal to

$$\Delta s_{sh} = s(h_B, P_B) - s(h_A, P_A), \tag{31}$$

where h_B and P_B result from solving the RH relations for a nonideal compressible flow. The upstream state P_A and M_A is related to the values of pressure and Mach in section 1, and the correlation is found using the results of CFD simulations of the supersonic flow in radial stators operating in over- and under-expanded conditions (Cappiello et al., 2022).

To assess the sensitivity of the shock losses to different pre-shock conditions and shock-wave angle, the entropy generation across an oblique shock wave inclined at 45° has been computed as a function of the pre-shock Mach number M_A and compared to that of a shock-wave whose inclination angle depends on the upstream Mach number in accordance to Equation 30. The results are plotted in Figure 4. The trend of the shock angle ε with the upstream Mach M_A is also displayed on the right hand side y-axis of Figure 4. It can be observed that the entropy generation is largely dependent on the value of the inclination angle, and that the use of a fixed shock angle in a ROM for turbomachinery design can lead to a significant overestimation of the associated shock losses.

The accuracy of the first-principle shock loss model has been verified against results from a two-dimensional CFD simulation. Table 1 reports the comparison of the computed entropy change with the two models for a case of supersonic nozzle flow passing through a normal shock, highlighting that the results between the two models are very similar.

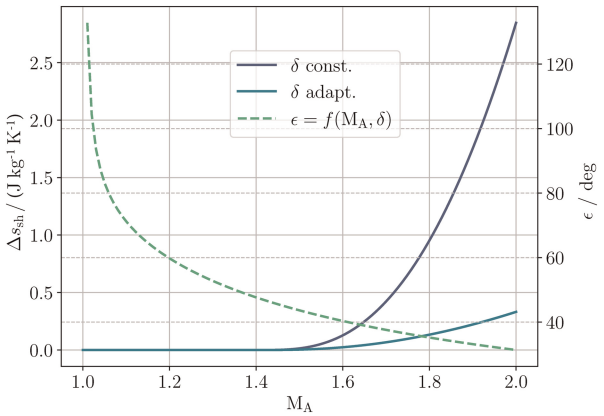

Figure 4. On the left *y*-axis: entropy change obtained by solving the RH governing equations (solid lines) as a function of the pre-shock Mach number M_A assuming (i) a constant shock angle $\varepsilon = 45°$, and (ii) a varying shock angle as a function of M_A (Equation 30). On the right *y*-axis: shock angle ε as a function of M_A (dashed line).

Table 1. Entropy change across a normal shock in a flow through a planar nozzle calculated with an inviscid 2D CFD model and comparison with the solution of the RH equations.

Model	$\Delta s/(\mathrm{J\ kg^{-1}\ K^{-1}})$	P_B/bar	$\mathrm{M_B}$
CFD	16.35	9.92	0.552
ROM	16.94	9.79	0.552

In both cases, the pre-shock conditions are $P_A = 2.93$ bar and $\mathrm{M_A} = 1.84$ and the fluid is Siloxane MM.

Radial gap loss

Losses in the radial gap are attributed to viscous friction on the endwalls and the associated entropy generation can be expressed as (Whitfield and Baines, 1990)

$$\Delta s_{rg,ew} = s(h_2, P_2) - s_1, \tag{32}$$

where h_2 can be determined from the energy conservation $h_2 = ht0 - (V_{\theta 2}^2 + V_{m2}^2)/2$.

$V_{\theta 2}$ can be calculated In accordance to Equation 33 as

$$\frac{V_{\theta 1}}{V_{\theta 2}} = \left[\frac{R_2}{R_1} + \frac{2\pi\ C_f \rho_2 V_{\theta 2}(R_1^2 - R_1 R_2)}{\dot{m}}\right], \tag{33}$$

in which the turbulent friction coefficient C_f is calculated as recommended in Equation 34

$$C_f = k\ (1.8 \cdot 10^5/\mathrm{Re})^{0.2}. \tag{34}$$

Equation 33 is solved in combination with 14 and 16 to find the flow state at the outlet of the radial gap. A value $k = 0.0035$ was used, determined by comparison with results of RANS simulations (Cappiello et al., 2022) of the flow in radial turbine stages featuring gap ratios $R_1/R_2 \in (1.03, 1.24)$ and operating with siloxane MM as working fluid. Figure 5 shows the trend of tangential velocity ratio obtained with the CFD and the reduced order model for two values of k.

Impeller loss

Loss sources in the impeller are assumed to be predominantly related to passage and tip leakage flow. Passage flow losses are due to viscous dissipation in the boundary layers, and to mixing of the passage vortex. The semi-empirical model proposed by Baines (1998), accounting for viscous, blade loading and secondary flow losses, is

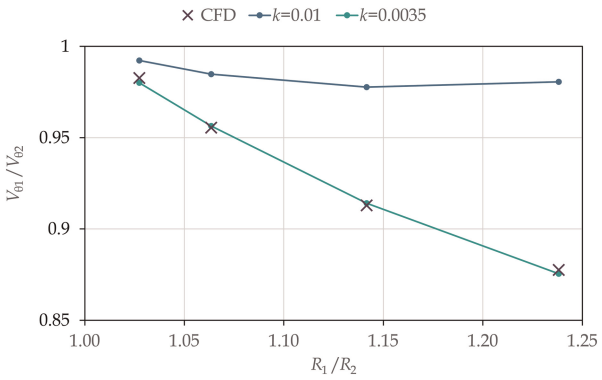

Figure 5. Variation of the tangential velocity ratio as given by Equation 33 for two values of k (solid lines) and comparison with CFD results (×).

used in this work to compute the passage losses. The model, reported in Equation 35, has been shown to be more accurate of that of Rodgers documented in Whitfield and Baines (1990) for predicting the efficiency of supersonic ORC RITs by Manfredi et al. (2021).

$$\Delta h_{\text{pass}} = K_p \left\{ \left(\frac{L_H}{D_H} \right) + 0.68 \left[1 - \left(\frac{\bar{R}_3}{R_2} \right)^2 \right] \frac{\cos\beta_{3g}}{b_3/c} \right\} \cdot \frac{1}{2} (W_2^2 + W_3^2). \tag{35}$$

In Equation 35, c is the blade chord, z the impeller axial length, L_H the hydraulic length, and D_H the hydraulic diameter.

Losses due to tip leakage flow are computed in accordance to Baines (1998)

$$\Delta h_{\text{leak}} = \frac{U^3 N}{8\pi} \left(K_x \varepsilon_x C_x + K_r \varepsilon_r C_r + K_{xr} \sqrt{\varepsilon_x \varepsilon_r C_x C_r} \right). \tag{36}$$

In Equation 36, ε_x is the axial and ε_r the radial tip gap, K_x, K_r and K_{xr} are the discharge coefficients, assumed constant, and C_x and C_r are parameters depending on the impeller configuration, whose definitions and values are reported in the Appendix A together with those of L_H and D_H. The entropy change across the impeller is finally computed as

$$\Delta s_{\text{imp}} = s(h_{3,is} + \Delta h_{\text{pass}} + \Delta h_{\text{leak}}, P_3) - s_2. \tag{37}$$

Diffuser loss

The losses occurring within the diffuser, assumed to be of conical shape, are computed by resorting to the model proposed by Agromayor et al. (2019). The governing equations are formulated as an implicit system of ordinary differential equations that are solved iteratively. The diffuser cant angle, the wall semi-aperture angle and the diffuser area ratio are specified as inputs, as well as the geometry and the flow state at the exit section of the impeller. Viscous flow losses in the diffuser are computed by specifying the friction factor. In this work this was fixed to 0.1 (Agromayor et al., 2019).

Model verification

In order to verify the accuracy of *TurboSim*, the results of the model have been compared with those obtained from CFD simulations. Two radial-inflow turbine test cases have been considered. The first test case consists of a high-pressure ratio RIT used as gas generator in the T100 turbo-shaft engine, designed and tested by Sundstrand Power Systems (Jones, 1996). The second test case is the so-called ORCHID turbine, representative of an ultra-high pressure ratio, single stage RIT for experimental research on high temperature ORC systems. The stage has been designed and optimized by means of high-fidelity CFD methods by De Servi et al. (2019).

CFD setup

The three-dimensional geometry of the T100 was constructed based on data from the open literature (Sauret, 2012) and the discretization of the three-dimensional geometry was performed using a commercial software (Ansys® CFX, n.d.). Unsteady, single-passage, RANS computations were used to predict the turbine performance, using a structured mesh comprising about 3 million cells. The optimal cell count of the stator, impeller, and diffuser was informed from a mesh sensitivity study (Matabuena, 2023) based on the Richardson extrapolation method (Roache, 1998). For the ORCHID turbine, a mesh of approximately 4 million cells was used to discretize the computational domain, as suggested in Cappiello et al. (2022). In this case, the computational domain only comprised the mesh of the convergent-divergent vane and that of the impeller.

For both test cases, the Ansys® CFX (n.d.) flow solver was employed. The discretization of the advection terms was performed using a central differencing scheme (CDS), ensuring a second order accurate solution. Turbulence closure was obtained through the Shear Stress Transport (SST$k-\omega$) model, and the turbulence equations were discretized using a hybrid scheme (Barth and Jespersen 1989). The uRANS equations were marched in time using a 1st order backward Euler scheme and the time transformation method (Giles, 1988) was employed to perform single-passage calculations with uneven pitch ratios, and imposing sliding interfaces

between the stationary and the rotating components. The total time of the simulation was set to one impeller passing period, subdivided into 100 time-steps. For each case, the computation was run until a time-periodic flow solution was achieved, by monitoring the value of the Mach number at the exit of the impeller blade passage at three different span-wise locations. The boundary conditions were imposed in terms of total thermodynamic conditions and flow direction at the inlet, and average static pressure at the outlet, see Table 2. For the T100, the average static pressure was specified at the diffuser exit section, while for the ORCHID at the impeller outlet section. The shroud wall was treated as a counter-rotating wall moving at the specified rotational speed.

Performance comparison

Table 3 reports the predictions of the turbine power and total-total efficiency obtained with *TurboSim* and with the CFD. The deviation in the efficiency values is within 1% for both cases. For the T100, the experimentally measured efficiency (Jones, 1996) is also reported. It can be observed that the CFD over-predicts the efficiency by 4%. A possible cause of discrepancy is due to the choice of not modeling the losses associated to the leakage flow from the hub.

Table 2. Boundary conditions and fluid models used in the uRANS simulations.

	T100	ORCHID
Fluid	Air	MM
EoS	Ideal-gas	MEoS
γ	1.4	1.025
$P_{t0}/(\text{bar})$	4.13	18.1
$T_{t0}/(K)$	477.6	573
Z_{t0}	1.0	0.738
$\bar{\gamma}_{Pv}$	1.4	0.952
$P_3/(\text{bar})$	0.724	0.443
$n/(\text{rpm})$	71700	98119

The thermodynamic conditions of the MM fluid have been computed using a look-up table (LUT) method. The LUT has been generated using the multi-parameter equation of state (MEoS) (Span and Wagner, 1996) implemented by Huber et al. (2022).

Table 3. Turbine performance prediction obtained with the ROM, CFD and experiments.

	T100[a]			ORCHID	
Quantity	ROM	CFD	Exp.	ROM	CFD
$\dot{w}/(\text{kW})$	66.3	69.8		10.1	10.2
$\eta_{tt}/(\%)$	91.2	92.1	87.1	84.9	85

The experimental data are available for the T100 only.
[a]Efficiency measured at the exit of the diffuser.

Further insights on the accuracy of the loss accounting methodology implemented can be gained by performing a loss breakdown analysis. The CFD-based loss breakdown was performed by mass-flow averaging the flow quantities at the inlet and outlet of each component in both time and space as

$$\bar{Q} = \frac{\sum_n^N \left(\left[\sum_{\tau=0}^{10t} q(\tau) \right]^n \cdot \rho^n \cdot V_m^n \cdot A^n \right)}{\dot{m}}, \tag{38}$$

where q is a generic time and space dependent thermo-physical quantity, τ is a specific time instant and t corresponds to a passage period, thus $t = 100 \cdot \tau$. The term $\rho^n \cdot V_m^n$ is the mass flux across the nth cell boundary, of area A^n.

By applying Equation 38 to calculate the space-time averaged isentropic outlet temperature and the entropy change across each component, the efficiency deficit can be calculated as

$$\Delta\eta = \frac{T_{\text{out},is}\ \Delta s}{\Delta h_{tt,is}}. \tag{39}$$

where $\Delta h_{tt,is}$ is the isentropic work, also computed averaging the enthalpy using Equation 38.

Figure 6a and 6b show the results of the loss breakdown analysis performed with the two models. The efficiency penalty across the stator and the impeller are displayed, along with the loss associated to the exit kinetic energy. The outcome of the loss breakdown analysis qualitatively shows that *TurboSim* predicts efficiency values close to those of the CFD. Notably, the ROM successfully captures the lower efficiency of the ORCHID turbine, which is characterized by a comparatively much higher pressure ratio. Minor deviations between the two models arise when comparing the share of loss of each turbine component, especially concerning the impeller losses which are overestimated by the ROM. In spite of the differences in the results illustrated in the plot, the accuracy of *TurboSim* is deemed adequate for systematic studies aimed at establishing guidelines for the design of *hiTORC-RIT*.

Results

TurboSim is used to generate design maps, namely contours and charts of key performance metrics as function of the most relevant independent variables of Equation 3. In particular, the influence of ψ_{is}, $\phi_{2,is}$, $\bar{\gamma}_{Pv}$, VR, and μ on the total-total and total-static stage efficiency is investigated. The size parameter SP, as defined by Perdichizzi and Lozza (1987), was fixed to 0.025 m in the study, a value typical of turbines for small-scale high-temperature ORC applications (De Servi et al., 2019; Manfredi et al., 2023). For size parameters different from that considered, the work of Manfredi et al. (2023) provides a complete treatment of its impact on efficiency. Constant geometrical scaling parameters, whose values are listed in Appendix C, were used to perform the design of the RITs. To attain a fixed value of SP for all designs, the mass flow rate was adjusted for each combination

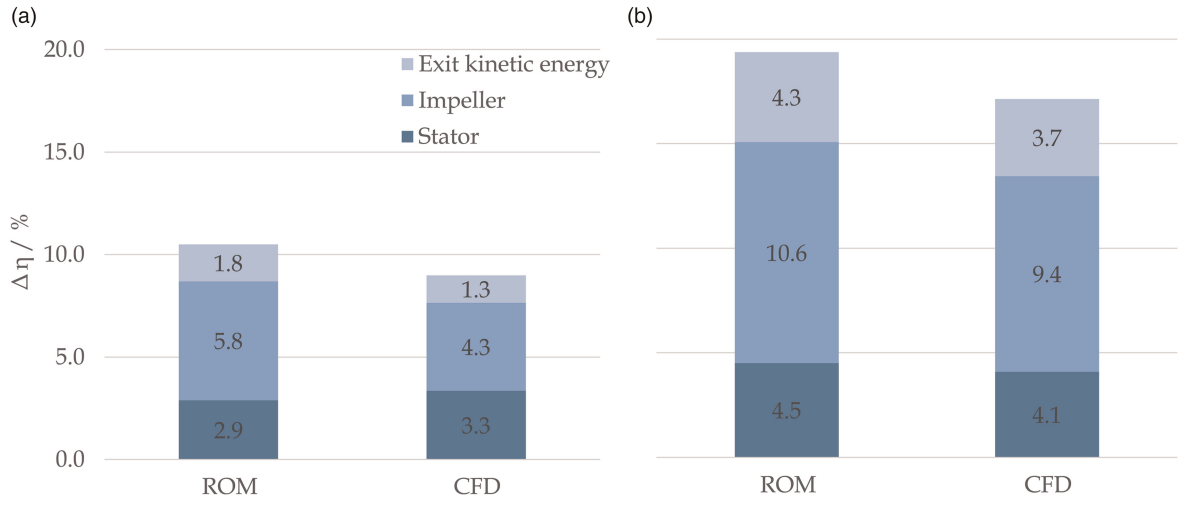

Figure 6. Loss breakdown obtained from calculation with *TurboSim* (ROM) and CFD. (a) T100 turbine. (b) ORCHID turbine.

of VR, $\bar{\gamma}_{Pv}$, and fluid. The size parameter is defined as

$$SP = \frac{\sqrt{\dot{Q}_{3,is}}}{\Delta h_{tt,is}^{0.25}}, \tag{40}$$

where $\dot{Q}_{3,is}$ is the volumetric flow rate at the stage outlet in isentropic conditions, and $\Delta h_{tt,is}$ is the isentropic work. Equation 40 can be rearranged considering $VR = \rho_{t0}/\rho_{3,is}$, $\dot{m} = \dot{Q}_{3,is} \cdot \rho_{3,is}$, and $\Delta h_{tt,is} = \psi_{is} \cdot U_2^2$, yielding

$$SP = \frac{\sqrt{\dot{m}\ VR}}{\sqrt{\rho_{t0}}(\psi_{is} \cdot U_2^2)^{0.25}}. \tag{41}$$

This relation was used to compute the mass flow rate $\dot{m}$, given SP, ψ_{is} and VR, and the total thermodynamic quantities at the inlet of the stage.

It should be noted that U_2 depends on the fluid characteristics, notably the speed of sound, according to the relation $U_2 = \mathrm{M}_{U_2} \cdot a_2$, where M_{U_2} is the tip peripheral Mach number. Because complex molecule fluids feature comparatively low speed of sound, the peripheral speed and the isentropic work of stages designed for such compounds are lower than for stages operating with fluids made of simple molecules. Consequently, for a given SP, the mass flow rate of stages operating with HMC fluids is inevitably larger. This results in a variation of turbine power in the investigated design space, ranging from tens of kW for turbines operating with HMC fluids in combination with high values of VR and ψ_{is}, up to 550 kW for turbines designed for low molecular complexity (LMC) fluids in combination with low VR and ψ_{is}.

Influence of the working fluid and $\bar{\gamma}_{Pv}$ on stage efficiency

The influence of the working fluid and $\bar{\gamma}_{Pv}$ on total-static efficiency are investigated by varying $VR \in (6, 80)$. Inlet thermodynamic conditions $P_r \in (0.5, 1.4)$ and $T_r \in (0.8, T_{f,\max})$ have been considered to obtain $\bar{\gamma}_{Pv}$ values in the range 0.45–1.17. Figure 7 illustrates the total-static efficiency as function of $\bar{\gamma}_{Pv}$. A color plot was used to display the variation of fluid molecular complexity MC, which was evaluated as the number of active

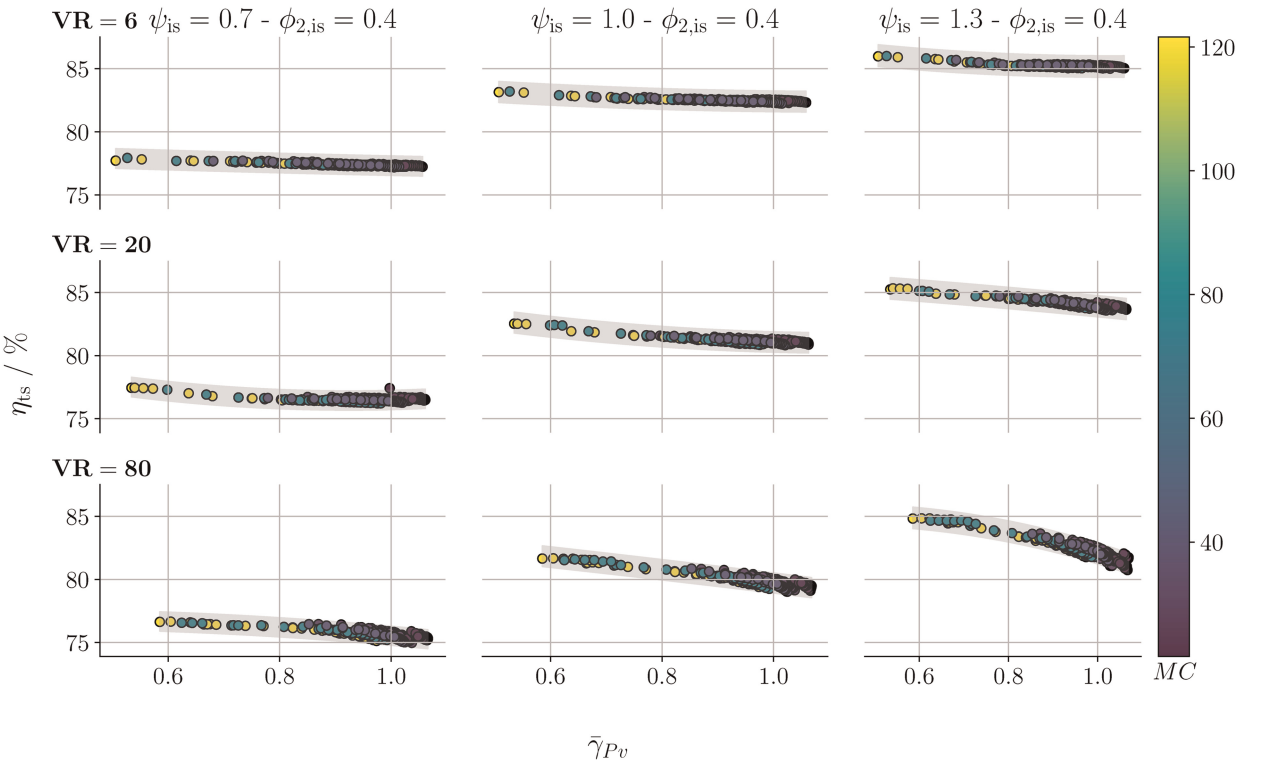

Figure 7. Total-static efficiency of RITs as a function of $\bar{\gamma}_{Pv}$ for working fluids of different molecular complexity MC. $SP = 0.025$ m, while $VR = 6$, 20 and 80 from top to bottom. ψ_{is} is equal to 0.7, 1.0 and 1.3 from left to right, and $\phi_{2,is}$ was fixed to 0.4. The gray bands indicate a $\pm 1\%$ uncertainty interval around the arithmetic average.

degrees-of-freedom of the molecule at its critical temperature (Harinck et al., 2009). The working fluids selected to generate the plots belong to the HMC class and are listed in Table 4 along with their MC and γ in dilute gas conditions.

The plots show that the efficiency decreases as the value of $\bar{\gamma}_{Pv}$ approaches that of γ, and the decrease is more appreciable for larger values of the volumetric flow ratio. For low values of VR the efficiency of turbines designed for fluids with different MC does not vary, therefore the variation of the fluid molecular complexity and of $\bar{\gamma}_{Pv}$ are not affecting the stage fluid-dynamic performance. For intermediate and large values of VR there is a marginal effect of the MC on efficiency: the efficiency value lies within a $\pm 1\%$ uncertainty interval around the arithmetic average, shown with gray bands in Figure 7. The impact of the variation of ψ_{is} was furthermore examined for $\phi_{2,is}$ equal to 0.4. Notably, it can be observed that the efficiency increases as ψ_{is} is increased, and the efficiency curves become steeper the larger the load. The reason why the turbine is more efficient when designed at higher ψ_{is} is explained in the following. All these results suggest that the impact of $\bar{\gamma}_{Pv}$ on efficiency is more significant at large volumetric flow ratios and loads, as visible in the bottom right plot of Figure 7.

To better display the role of $\bar{\gamma}_{Pv}$ to turbine efficiency, the efficiency of turbines computed considering the fluids and the inlet thermodynamic conditions listed in Table 5 is further investigated. Three expansions of MM up to $VR = 20$ and starting from the initial conditions listed in Table 5 were plotted in the reduced pressure and temperature diagram of Figure 8. An LMC fluid in the dilute gas state has been included in the analysis and reported in the same table. Paradigmatic examples of RITs operating with LMC fluids in dilute gas state are turbochargers and gas turbines. Plots of the total-total and total-static efficiency against the work coefficient ψ_{is} are displayed in Figures 9 and 10. Figure 9 shows the variation of efficiency with three values of VR, and for a fixed $\phi_{2,is}$ of 0.4. Similarly, Figure 10 illustrates the impact of $\phi_{2,is}$ on stage efficiency for $VR = 20$. The curves have been obtained by averaging the efficiency predicted at each value of ψ_{is} for siloxane MM and the LMC fluid in

Table 4. Fluids used to generate the data displayed in Figure 7 and their main characteristics.

Fluid name	Chemical name	MC	γ
Ethanol	Ethyl alcohol	21.51	1.080
Butane	n-Butane	29.53	1.054
Pentane	–	39.80	1.040
MM	Hexamethyldisiloxane	78.35	1.026
Dodecane	–	121.63	1.018

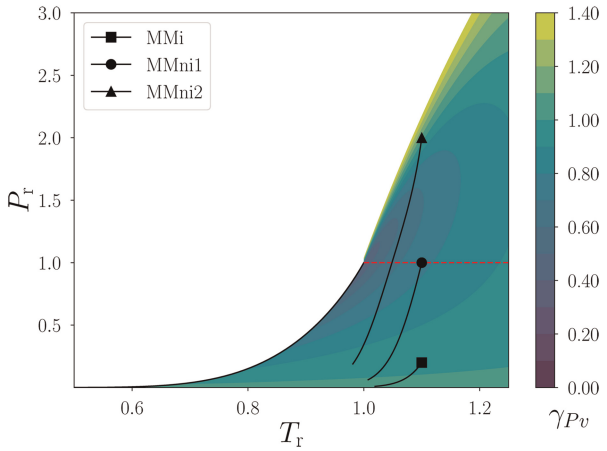

Figure 8. Reduced $P-T$ diagram for MM showing γ_{Pv} contours and three paradigmatic expansions at $VR = 20$, and starting from the inlet conditions listed in Table 5, namely MMi (□), MMni1 (◯), and MMni2 (Δ).

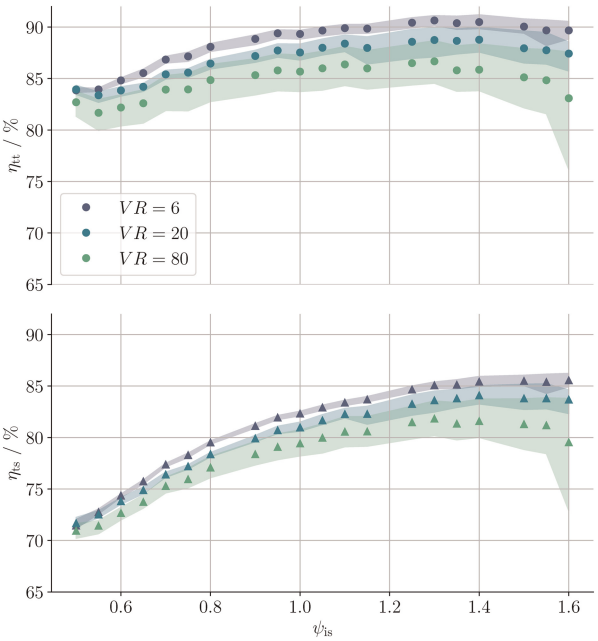

Figure 9. Total-total (◯) and total-static (Δ) efficiency as a function of the load coefficient ψ_{is}, for different values of VR and for a fixed value of the flow coefficient $\phi_{2,is} = 0.4$. The markers indicate the average value of efficiency computed for the cases listed in Table 5, while the colored bands show the min-max variation of the efficiency for $\bar{\gamma}_{Pv}$ that varies between 0.78 and 1.15.

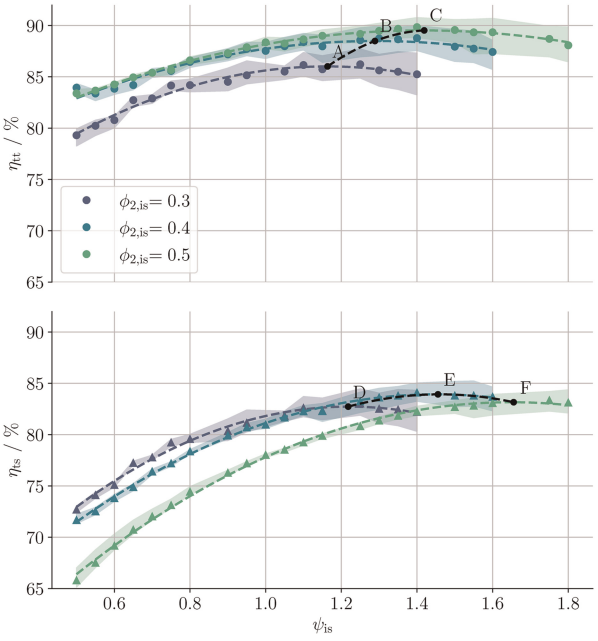

Figure 10. Total-total (◯) and total-static (Δ) efficiency as a function of the load coefficient ψ_{is}, for different values of $\phi_{2,is}$ and for a fixed value of the expansion ratio $VR = 20$. The colored markers indicate the average value of efficiency computed for the cases listed in Table 5, while the colored bands show the min-max variation of the efficiency for $\bar{\gamma}_{Pv}$ that varies between 0.78 and 1.15. The black dots display the values of the maxima at different values of $\phi_{2,is}$ estimated by fitting the data with a 2^{nd} order polynomial, shown by the colored dashed lines. The black dashed curves are 2^{nd} order polynomials fitting the optimal combinations of ψ_{is} and $\phi_{2,is}$.

the thermodynamic conditions listed in Table 5. The colored bands depict the min-max variation around the average, with the turbines designed for expansions characterized by high $\bar{\gamma}_{Pv}$ featuring the lowest efficiency values, in accordance with the results displayed in Figure 7. The main conclusion that can be drawn by

Table 5. Boundary conditions for the turbine operating with the LMC and the HMC (siloxane MM) fluid.

	MC	$P_{t0,r}$	$T_{t0,r}$	Z_{t0}	$\bar{\gamma}_{Pv}$
LMC	7.0	0.2	4.0	1.0	1.15
MMi	78.35	0.2	1.1	0.95	1.0
MMni1	78.35	1.0	1.1	0.71	0.92
MMni2	78.35	2.0	1.1	0.43	0.78

MMi denotes siloxane MM in ideal gas conditions, while MMni1 and MMni2 refer to MM conditions in the nonideal thermodynamic regime.

inspecting the plots is that the value of the optimal work coefficient is weakly dependent on *VR*, while it is affected by the value of $\phi_{2,is}$.

Loss breakdown analysis

Insight into the impact of the duty coefficients $\phi_{2,is}$, ψ_{is} on loss mechanisms is gained by examining the design layout of the optimal stages labeled with A, B and C in Figure 10, and the corresponding loss breakdown. From theoretical considerations, it can be demonstrated that the degree of reaction r^* decreases for increasing values of $\phi_{2,is} - \psi_{is}$. As r^* decreases, the enthalpy drop across the impeller reduces, along with the density variation. Lower density variation leads to a lower impeller outlet/inlet area ratio A_3/A_2, as illustrated in Figure 11a. The same figure also reports the values of A_3/A_2 and r^* for each of the three configurations. Moreover, Figure 11b shows that both absolute and relative flow angles at the outlet decrease from A to C, ultimately affecting losses and efficiency. Figure 12 illustrates the efficiency penalty associated to each of the loss mechanisms occurring in the stages. Because the leakage loss is inversely proportional to $\cos\beta_3$ (Denton, 1993), lower values of the outlet flow angle entail lower tip leakage losses for case C, as confirmed by the analysis. On the contrary, being directly proportional to $\cos\beta_3$, see Equation 35, profile losses are lower for case A.

To further clarify the effect of $\bar{\gamma}_{P_v}$ on loss mechanisms, trends of the Mach numbers at the exit of the stator and of the impeller for turbines operating with fluids in the conditions reported in Table 5 are shown in Figure 13. One can notice that stages characterized by lower values of $\bar{\gamma}_{P_v}$ yield the lowest Mach numbers at the outlet of both components. Lower cascade outlet Mach numbers leads to reduced fluid-dynamic losses, as confirmed by the trends of the efficiency penalty $\Delta\eta$ illustrated in Figure 14.

Figure 15 reports the results of the loss breakdown analysis for the stator and the impeller of two turbines designed for the cases LMC and MMni2, featuring $\psi_{is} = 1.35$, $\phi_{2,is} = 0.4$ and $VR = 20$. The share of mixing losses for both the stator and impeller is very similar between the LMC and MMni2 cases, due to the opposite influence of $\bar{\gamma}_{P_v}$ and Mach number on loss, which could also be inferred by the right hand plot of Figure 1. Similar conclusions on mixing losses were drawn by Tosto et al. (2022), who showed that stages operating with fluid molecules characterized by different complexity, or operating in the nonideal thermodynamic regime, feature comparable values of mixing losses when operating at the same *VR*. Endwall and profile losses mainly depend on the Mach number and flow angle, and are less relevant for the MMni2 case due to the lower exit Mach numbers.

Influence of the meridional velocity ratio on efficiency

A design parameter which largely affects the turbine layout and whose optimal value for *hiTORC-RIT* is not reported in the literature is the meridional velocity ratio of the impeller, herein denoted with μ. An investigation is therefore carried out to gain insight on its impact on stage efficiency and turbine design. Design maps are computed for $\mu = 1.2, 1.4, 1.6$. In this case, *VR* was set to the nominal value of the ORCHID turbine, along with the other design parameters listed in Appendix C. The working fluid is siloxane MM, and the stage boundary conditions are those previously listed in Table 2. Figure 16 shows the isolines of the total-total efficiency, whereas Figure 17 displays those of total-static efficiency. The efficiency values reported in the charts indicate that the meridional velocity ratio marginally affects the maximum η_{tt} and η_{ts}, and the only appreciable effect is related to the width and location of the region of optimal designs. Considering the value of η_{tt}, the isoline

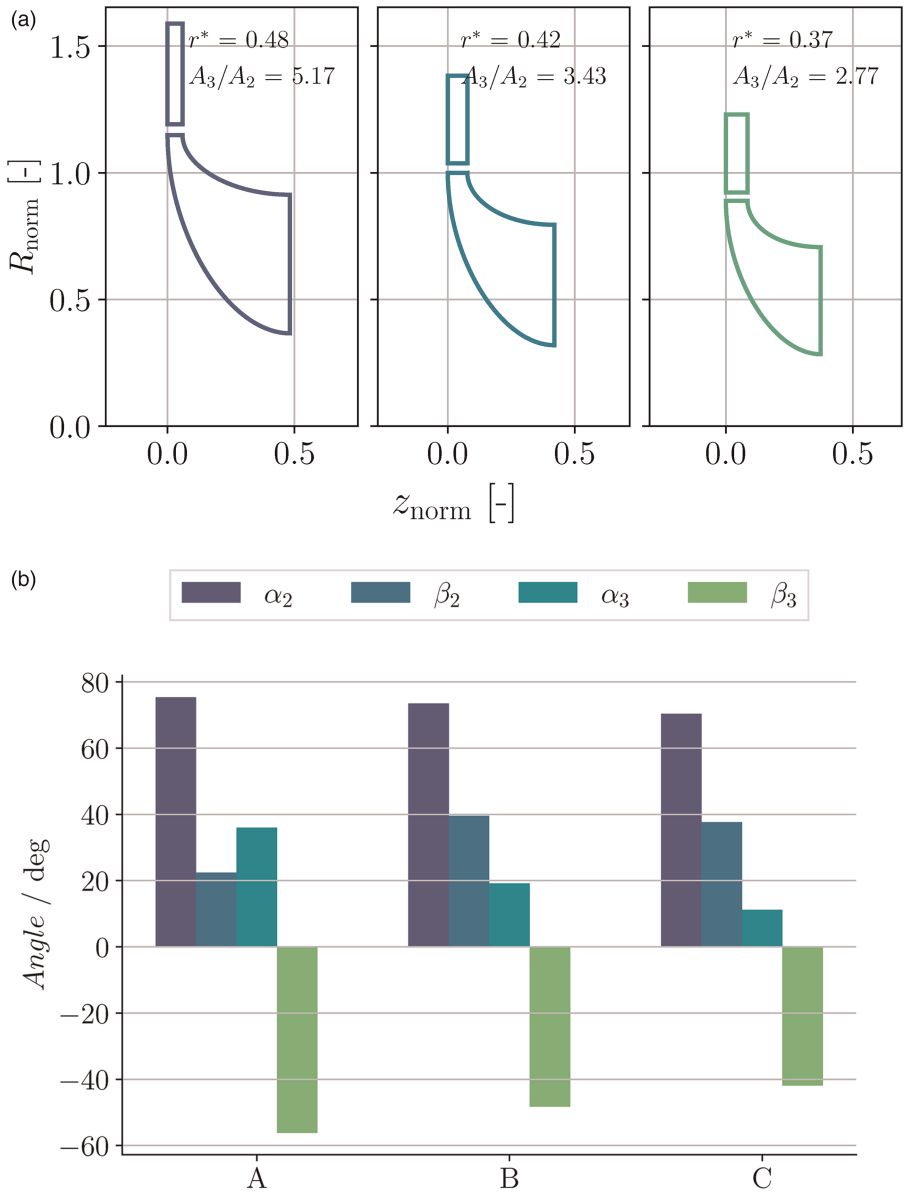

Figure 11. (a) Meridional flow path of the optimal designs A, B and C of Figure 10. The axial and radial coordinates are non-dimensionalized by the tip radius of case B. (b) Impeller absolute flow angles (α) and relative flow angles (β) for the A, B and C cases.

corresponding to the optimum designs shifts towards lower $\phi_{2,is}$ as μ is increased. The same change occurs to the isoline delimiting the designs featuring the highest η_{ts}. The red markers on the total-total and total-static efficiency maps for $\mu = 1.4$ indicate the design point of the ORCHID turbine and the calculated η_{tt} and η_{ts}.

Design guidelines

The results that have been used to generate the maps are finally converted in design guidelines, namely charts that can be used to quickly size the turbine and compute its efficiency in system-level analysis and optimization. A relevant example in which such a model is exploited is reported in Krempus et al. (2023).

Figure 18 shows the trend of maximum η_{tt} and η_{ts} as a function of $VR \in (3, 80)$ for the four cases listed in Table 5. The duty coefficients ϕ_2, ψ corresponding to the maximum efficiency point at each value of VR are displayed in the left hand side graphs, while the corresponding values of the efficiency are shown on the right hand side.

The optimal flow coefficient ϕ_2 value remains unchanged above $VR \simeq 10$, represented in the figure using triangular markers. The optimal ϕ_2 value to maximize η_{tt} is ≈ 0.52, while $\phi_2 \approx 0.43$ should be selected to size

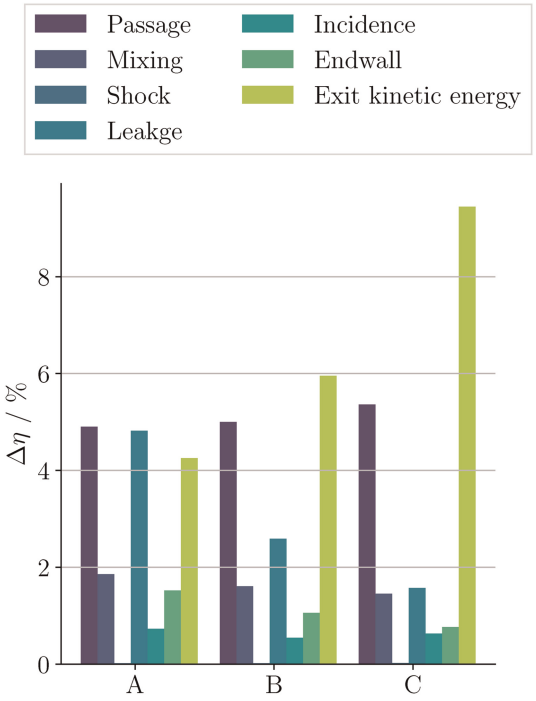

Figure 12. Stage (stator + impeller) loss breakdown for optimum designs A, B and C shown in Figure 10. The optimal work coefficients are, respectively, 1.15, 1.3 and 1.4. Results obtained for $VR = 20$.

the turbine for maximum η_{ts}. By comparing the left hand side plots of the Figure 18a–18d, one can notice that the optimal ϕ_2 is not affected by change in the value of $\bar{\gamma}_{Pv}$.

On the contrary, the optimal load coefficient ψ (marked by crosses) shows appreciable differences when $\bar{\gamma}_{Pv}$ varies. At low VR, the optimum $\psi \approx 1.3$ for either maximum η_{tt} and η_{ts}, regardless of the value of $\bar{\gamma}_{Pv}$. As VR increases up to values between 10 and 20 depending on $\bar{\gamma}_{Pv}$, ψ increases. This result is in accordance with the findings of Da Lio (2019), who also observed that the optimal design load coefficient increases as VR increases from 2.3 to 8.7 for turbines of similar scale and operating with R245fa as working fluid. However, as VR is further increased, the value of load coefficient that maximizes η_{tt} decreases to $\psi \approx 1.15$ in Figure 18a for the LMC case, and $\psi \approx 1.3$ for the MMi case in Figure 18b. For the cases MMni1 and MMni2 of Figure 18c and 18d, whereby $\bar{\gamma}_{Pv} < 1$, the optimal $\psi \approx 1.35$ and 1.42.

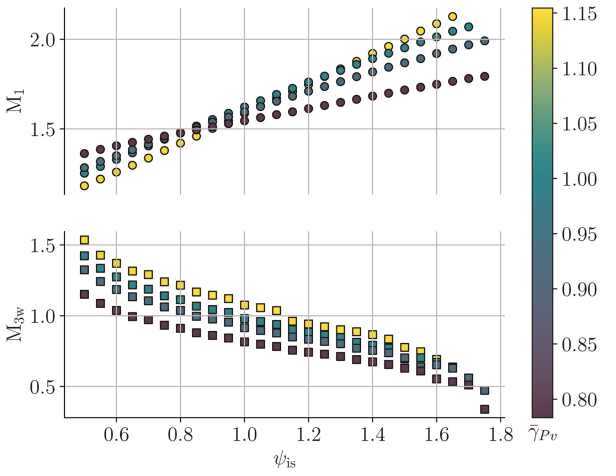

Figure 13. Absolute Mach number at the outlet of the stator (◯) and relative Mach number at the outlet of the impeller (□) as a function of the load coefficient ψ_{is}, for the LMC, MMi, MMni1 and MMni2 cases listed in Table 5 at fixed $VR = 20$, $SP = 0.025$ m, and $\phi_{2,is} = 0.4$.

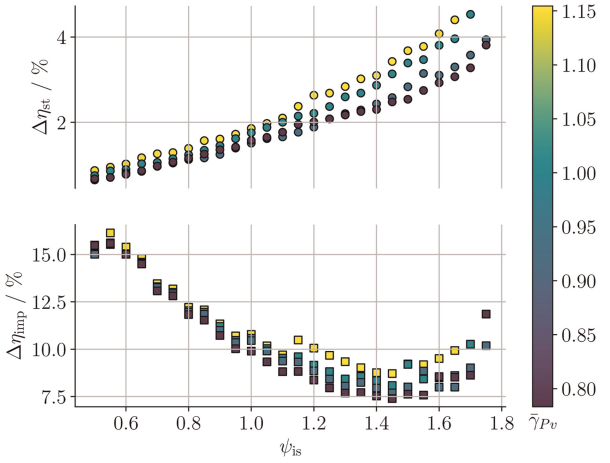

Figure 14. Cumulative stator (◯) and impeller (□) loss as a function of the load coefficient ψ_{is}, for the LMC, MMi, MMni1 and MMni2 cases listed in Table 5 at fixed $SP = 0.025$ m, $SP = 0.025$ m, and $\phi_{2,is} = 0.4$.

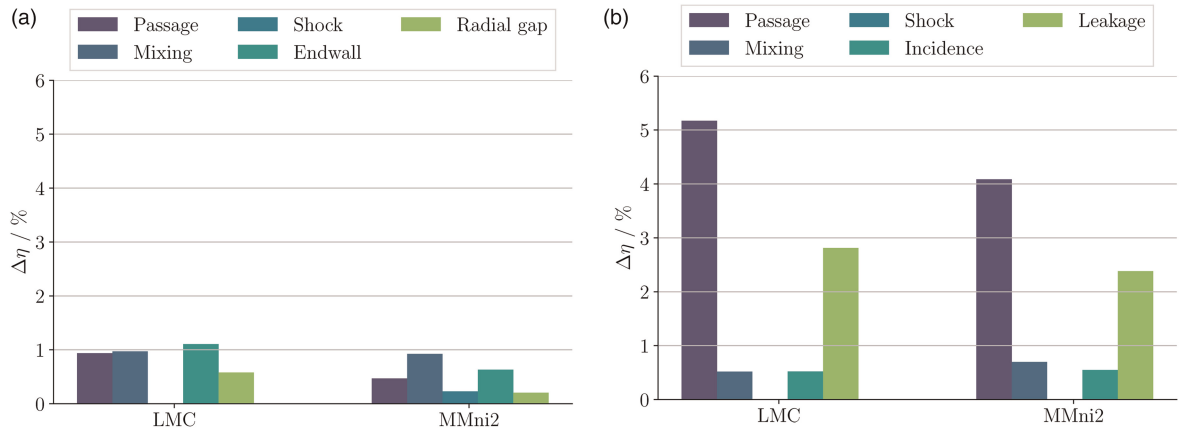

Figure 15. Loss breakdown in the stator (a) and the impeller (b) for the LMC and MMni2 cases listed in Table 5. $\psi_{is} = 1.35$, $\phi_{2,is} = 0.4$ and $VR = 20$. (a) Stator losses. (b) Impeller losses.

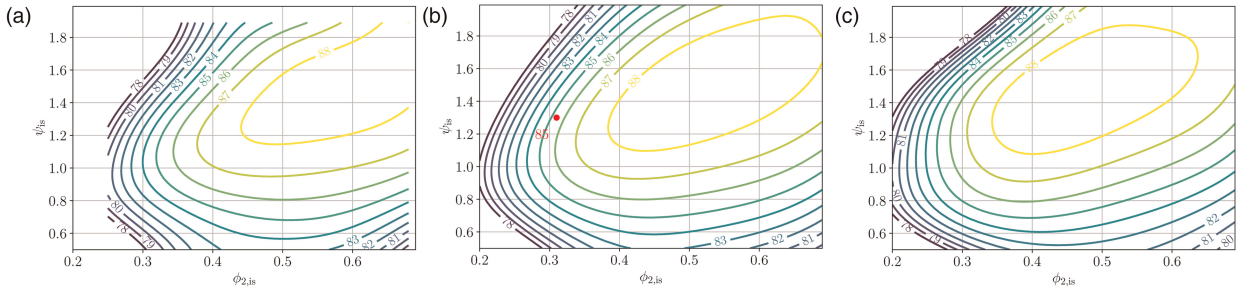

Figure 16. Design maps showing the contours of total-total efficiency of turbines operating at $VR = 49.7$, and for increasing values of μ. The fluid is siloxane MM. The red marker in (b) highlights the design point and efficiency of the ORCHID turbine. (a) $\mu = 1.2$. (b) $\mu = 1.4$. (c) $\mu = 1.6$.

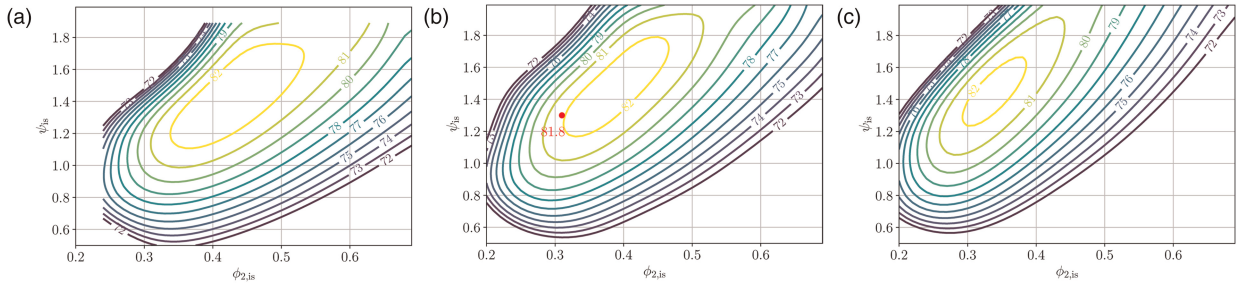

Figure 17. Design maps showing the contours of total-static efficiency of turbines operating at $VR = 49.7$, and for increasing values of μ. The fluid is siloxane MM. The red marker in (b) highlights the design point and efficiency of the ORCHID turbine. (a) $\mu = 1.2$. (b) $\mu = 1.4$. (c) $\mu = 1.6$.

A similar trend occurs with the value of ψ that maximizes η_{ts}, although the change with $\bar{\gamma}_{Pv}$ is less pronounced and ψ varies between 1.3 and 1.45 from Figure 18a–18d. The trends shown in Figure 18 also highlight that the value of the optimal ψ for maximum η_{tt} is very similar to that guaranteeing maximum η_{ts} when $\bar{\gamma}_{Pv} < 1$.

In summary, when designing RITs operating with fluids in thermodynamic states for which $\bar{\gamma}_{Pv} \geq 1$ and $VR < 10$, as in the case of turbine stages operating with LMC fluids in close to dilute gas conditions, one may choose ψ, $\phi_2 \approx (1.3, 0.52)$ for optimal η_{tt}, and ψ, $\phi_2 \approx (1.3, 0.35)$ for optimal η_{ts}. Conversely, when designing machines for which the fluid states lead to $\bar{\gamma}_{Pv} < 1$ and $VR > 10$, as for turbines of high-temperature ORC power systems, one should select ψ, $\phi_2 \approx (1.43, 0.52)$ for optimal η_{tt}, and ψ, $\phi_2 \approx (1.45, 0.43)$ for optimal η_{ts}.

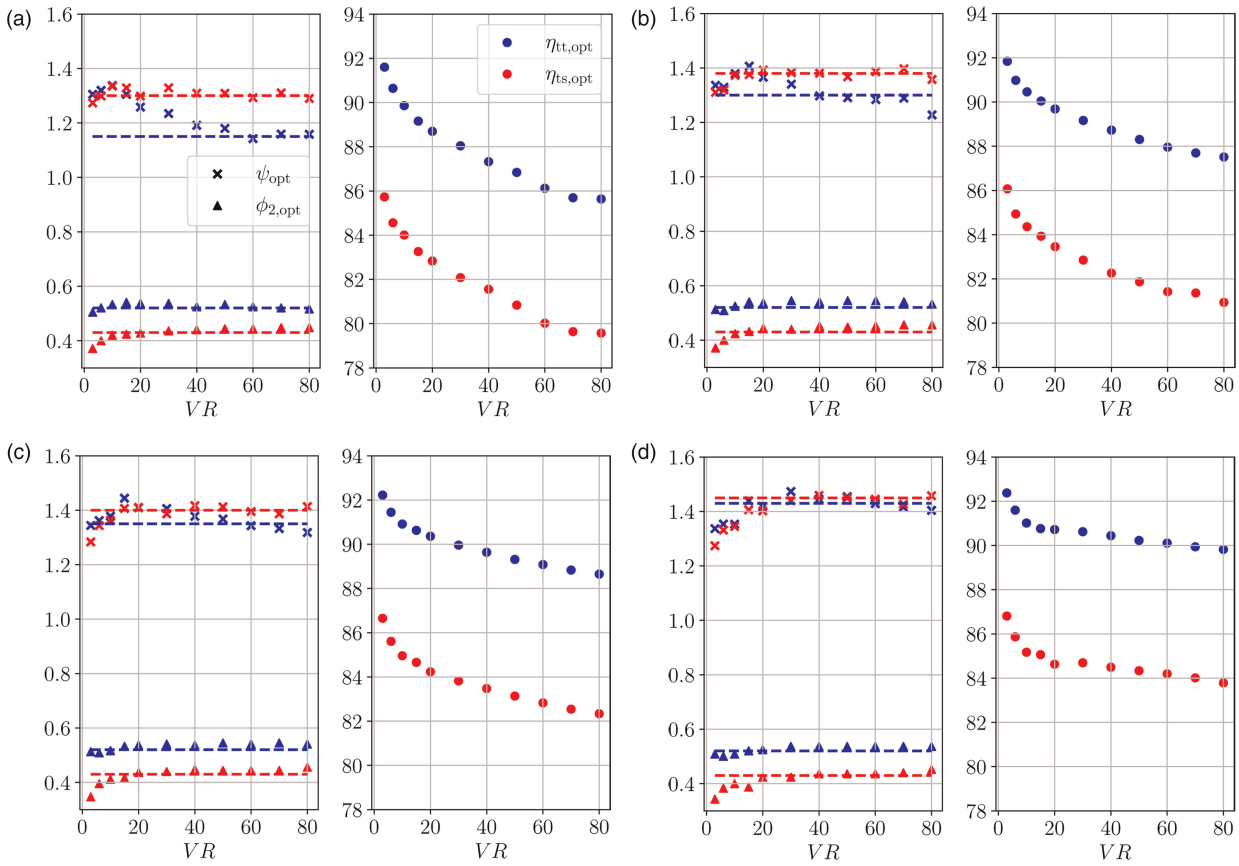

Figure 18. Optimal ψ (×) and ϕ_2 (Δ) as a function of *VR*, and corresponding maximum η_{tt} and η_{ts} as a function of *VR*. The blue markers indicate the duty coefficients that maximize η_{tt} and the red ones those that maximize η_{ts}. The results were obtained for the LMC, MMi, MMni1 and MMni2 cases listed in Table 5. (a) LMC case, $\bar{\gamma}_{Pv} = 1.15$. (b) MMi case, $\bar{\gamma}_{Pv} = 1.0$. (c) MMni1 case, $\bar{\gamma}_{Pv} = 0.92$. (d) MMni2 case, $\bar{\gamma}_{Pv} = 0.78$.

Considering the values of efficiency, both the optimal η_{tt} and the optimal η_{ts} decrease as *VR* is increased, as already established by other authors (Perdichizzi and Lozza, 1987; Da Lio, 2019; Manfredi et al., 2023). However, when comparing the efficiency for the four cases displayed in Figure 18, the highest values of the efficiency are obtained when $\bar{\gamma}_{Pv} < 1$ for any given *VR*. Furthermore, the efficiency drop observed at increasing *VR* values reduces for decreasing values of $\bar{\gamma}_{Pv}$.

Conclusion

Design guidelines for radial-inflow turbines of high-temperature organic Rankine cycle power systems are documented. The influence of the working fluid, nonideal thermodynamic effects, and of the volumetric flow ratio on the choice of optimal design parameters ψ, ϕ_2 and stage efficiency has been investigated. Values up to $VR = 80$ have been considered, while the size parameter was fixed to $SP = 0.025$ m, a value typical of RITs for high-temperature ORC systems up to few hundreds kW power capacity, depending on the working fluid. The guidelines have been derived by analyzing the results obtained with a reduced-order model for turbine design and performance assessment, and based on first principles. The accuracy of the reduced order model has been verified against high fidelity CFD simulations of two test cases representative a high pressure ratio gas turbines and a *hiTORC-RIT*. The main outcomes of this study can be summarized as follows:

- The efficiency predicted by the reduced-order model is within 1% the value obtained with uRANS. The model was able to correctly capture the effect of the volumetric flow ratio on the efficiency.
- The optimal value of duty coefficients ψ and ϕ_2 depends on the value of the volumetric flow ratio, and on the value of $\bar{\gamma}_{Pv}$ along the expansion process. RITs for high temperature ORC systems should be designed with ψ, $\phi_2 \approx (1.43, 0.52)$ for optimal η_{tt}, and ψ, $\phi_2 \approx (1.45, 0.43)$ for optimal η_{ts}.

- The values of the optimal duty coefficients derived in this work differ from those that can be inferred from the design maps of Rodgers (1987) and Chen and Baines (1994). Therefore, it can be argued that the application of conventional design maps can lead to sub-optimal *hiTORC-RIT* designs.
- Nonideal thermodynamic effects quantified through $\bar{\gamma}_{Pv}$ have an appreciable impact on turbine efficiency only for volumetric flow ratios higher than 10, while their influence is negligible at low values of *VR*.
- The results documented in this work extend the analysis provided in (Perdichizzi and Lozza, 1987; Da Lio, 2019; Manfredi et al., 2023) to volumetric flow ratios beyond 50. Similar conclusions related to the choice of the optimal load coefficient presented in (Da Lio, 2019) were found.
- The study offers new insights into why *hiTORC-RIT* operating in nonideal thermodynamic conditions can achieve relatively high efficiency, even when designed for very high volumetric flow ratio.

Albeit the investigation is focused on *hiTORC-RIT*, the derived guidelines can be applied to the preliminary design of radial-inflow turbines operating with arbitrary working fluids, at low to very high volumetric flow ratios, and in both ideal and nonideal thermodynamic regime. Future work will be devoted to extend the capability of the reduced-order model to off-design performance assessment, to the development of design guidelines for mixed-flow turbines, and to perform a campaign of experimental validation using the ORCHID facility at the Propulsion and Power laboratory of Delft University of Technology.

Nomenclature

Roman symbols

A	area (m^2)
b	passage height (m)
c	chord length (m)
C_D	dissipation coefficient
C_f	wall friction coefficient
$C_{P_b,\text{eff}}$	effective base pressure coefficient
C_r	exducer tip gap coefficient (XX)
C_x	inducer tip gap coefficient (XX)
D_H	hydraulic diameter impeller (m)
E	boundary layer energy factor
g_s	pitch (m)
G	array of geometrical characteristics (m)
h	enthalpy (J/kg)
H	boundary layer shape factor
K_p	impeller passage loss coefficient
K_r	exducer tip gap discharge coefficient
K_x	inducer tip gap discharge coefficient
K_{xr}	combined tip gap discharge coefficient
L_H	hydraulic length impeller (m)
L_x	axial length impeller (m)
$\dot{m}$	mass flowrate (kg/s)
M	Mach number
MC	Molecular complexity
n	rotational speed (rpm)
N	blade count impeller
P	pressure (bar)
P_b	base pressure (bar)
PR	pressure ratio
Q	critical kinetic energy ratio
r^*	degree of reaction
R	radius (m)
Re	Reynolds number
s	entropy [J/(kg·K)]

t thickness (m) or time (s)
T temperature (K) or period (s)
U peripheral velocity (m/s)
v specific volume (m^3/kg)
V absolute velocity (m/s)
VR volumetric flow ratio
w work (J/kg)
$\dot{w}$ power (W)
W relative velocity (m/s)
Z compressibility factor

Greek symbols

α absolute flow angle (deg)
β relative flow angle (deg)
γ specific heat ratio in the dilute gas limit
γ_{Pv} isentropic pressure-volume exponent
$\bar{\gamma}_{Pv}$ logarithmic average isentropic pressure-volume exponent
δ deviation angle across shock (deg)
δ^* boundary layer displacement thickness (m)
Δ variation
ε shock angle (deg)
ε_r exducer tip gap to blade height ratio
ε_x inducer tip gap to blade height ratio
ζ loss coefficient
η efficiency
θ boundary layer momentum thickness (m)
μ impeller meridional velocity ratio
ξ impeller cone angle (deg)
ρ density (kg/m^3)
σ solidity
$\boldsymbol{\sigma}$ array of geometrical design variables
τ time instant (s)
ϕ flow coefficient
ψ work or load coefficient

Subscripts

0 stator inlet section
1 stator outlet section
2 impeller inlet section
3 impeller outlet section
2D two-dimensional
A pre-shock
B post-shock
cr critical
ew endwall
g geometric
h hub
imp impeller
is isentropic
leak leakage
m meridional or mid-span
mo mixedout
mx mixing

out	outlet
pass	passage
prof	profile
r	reduced
s	shroud
sh	shock
st	stator
t	total
tt	total-total
ts	total-static
w	relative frame of reference
θ	tangential direction

Definitions

$$\psi_{is} = \frac{\Delta h_{tt,is}}{U_2^2}$$

$$\phi_{2,is} = \frac{V_{m2,is}}{U_2}$$

$$\psi = \frac{\Delta h_{tt}}{U_2^2}$$

$$\phi_2 = \frac{V_{m2}}{U_2}$$

Acronyms

EoS	equation of state
hiTORC-RIT	high-temperature organic Rankine cycle radial-inflow turbine
HMC	high molecular complexity
LMC	low molecular complexity
LUT	look-up table
MEoS	Multi parameter equation of state
NICFD	nonideal compressible fluid dynamics
ORC	organic Rankine cycle
ORCHID	organic Rankine cycle hybrid integrated device
RANS	Reynolds averaged Navier-Stokes
RH	Rankine-Hugoniot
RIT	radial-inflow turbine
ROM	reduced order model
uRANS	unsteady Reynolds averaged Navier-Stokes

Appendix A Coefficients of the Baines loss model for radial-inflow turbine impellers

The hydraulic length and diameter used to compute the impeller passage losses as per Equation 35 write as

$$L_H = \frac{\pi}{4}\left[\left(z - \frac{b_2}{2}\right) + \left(R_2 - R_{3s} - \frac{b_3}{2}\right)\right],$$

$$D_H = \frac{1}{2}\left[\left(\frac{2\pi R_2 b_2}{4\pi R_2 + 2Z_b b_2} + \frac{2\pi(R_{3s}^2 - R_{3h}^2)}{\pi(R_{3s} + R_{3h}) + 2Z_b b_3}\right)\right].$$

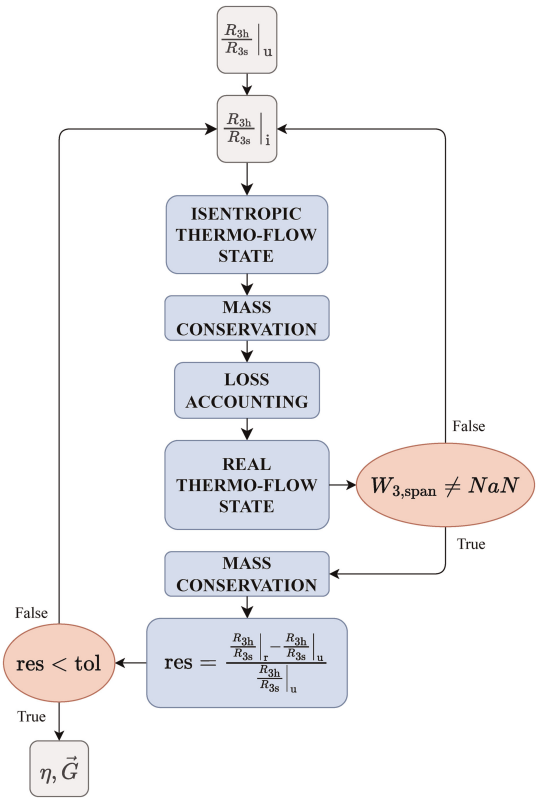

Figure 19. Stage sizing routine workflow.

Table 6. Values of the turbine design parameters fixed in the current investigation.

Variable	Value	Variable	Value
α_0	25°	σ_{st}	1.56
α_3	0°	$\frac{t}{g}\Big\|_1$	0.015
ξ_2	90°	$\frac{t}{g}\Big\|_3$	0.06
ξ_3	0°	$\frac{\epsilon_x}{b_2}$	0.1
$\frac{R_{3h}}{R_{3s}}$	0.4	$\frac{\epsilon_r}{b_3}$	0.16
$\frac{R_{3m}}{R_2}$	0.56	$\frac{V_{m3}}{V_{m2}}$	1.25
$\frac{R_2}{R_1}$	0.96	$\frac{\delta^*}{\theta}$	2.0
$\frac{R_1}{R_0}$	0.75	$\frac{\theta}{t_{TE}}$	0.075
$\frac{b_2}{b_1}$	1.0	C_D	0.002
$\frac{b_1}{b_0}$	1.0		
$\frac{\bar{b}}{\Delta R}\Big\|_{st}$	0.28		
$\frac{L_x}{\Delta R}\Big\|_{imp}$	0.95		

The coefficients C_x and C_r in Equation 36 are computed as

$$C_x = \frac{1 - (R_{3s}/R_2)}{V_{m2} b_2},$$

$$C_r = \frac{R_{3s}}{R_2} \frac{z - b_2}{V_{m3} \bar{R}_3 b_3}.$$

Appendix B Stage sizing routine in *TurboSim*

A stage sizing routine is implemented in *TurboSim* to determine the inlet and outlet section radii of the impeller and of the stator. With reference to Figure 19, the control parameter for the iterative method is the isentropic exducer radius ratio $R_{3h}/R_{3s}|_i$. The desired $R_{3h}/R_{3s}|_u$ is used to start the iterative calculation process. The program computes the isentropic thermodynamic state and the velocity triangles at each spanwise section and the flow path size is determined by imposing the mass conservation through each section of the machine. The loss accounting is performed based on the flow quantities, thermodynamic fluid properties, and geometry, that are updated at each iteration. The relative velocity at the exit section of the impeller is concurrently verified at each spanwise section to ensure that the obtained solution is physical. The actual exducer radius ratio $R_{3h}/R_{3s}|_r$ is finally calculated, and the convergence is reached once the value of the relative error with respect to the specified exducer radius ratio is lower than a given tolerance.

Appendix C Geometrical scaling parameters fixed in *TurboSim*

The geometrical scaling parameters for the design of the turbines investigated in this study are listed in Table 6.

Acknowledgments

Majer M. would like to acknowledge Dr. Andrea Giuffré for his precious advice on programming, numerical computation, and turbomachinery design. A heartfelt appreciation also goes to Lorenzo Galieti, whose ideas during long discussions helped interpret some of the results presented herein. Thanks to Luis Matabuena for generating and sharing the mesh of the T100 diffuser which was used in the CFD validation herein presented.

Funding sources

The research work was supported by the Dutch Technology Foundation TTW, Applied Science Division of NWO, the Technology Program of the Ministry of Economic Affairs (grant no. 17906). The financial and in-kind support of partner companies is also gratefully acknowledged.

Competing interests

Matteo Majer declares that he has no conflict of interest. Matteo Pini declares that he has no conflict of interest.

References

Agromayor R., Müller B., and Nord L. O. (2019). One-dimensional annular diffuser model for preliminary turbomachinery design. *International Journal of Turbomachinery, Propulsion and Power*. 4 (3).

AMES (1953). Equations, tables, and charts for compressible flow, Technical report, NACA.

Ansys® CFX (n.d.). Academic Research CFX, Release 22.0.

Bahamonde S., Pini M., Servi C. D., Rubino A., and Colonna P. (2017). Method for the preliminary fluid dynamic design of high-temperature mini-organic Rankine cycle turbines. *Journal of Engineering for Gas Turbines and Power*. 139 (8): 082606. https://doi.org/10.1115/1.4035841.

Baines N. C. (1998). A meanline prediction method for radial turbine efficiency, Technical report, Concepts ETI, Inc.

Barth T. and Jespersen D. (1989). The design and application of upwind schemes on unstructured meshes.

Baumgärtner D., Otter J. J., and Wheeler A. P. (2020a). The effect of isentropic exponent on supersonic turbine wakes. In International Seminar on Non-Ideal Compressible-Fluid Dynamics for Propulsion & Power, pp. 153–161.

Baumgärtner D., Otter J. J., and Wheeler A. P. S. (2020b). The effect of isentropic exponent on transonic turbine performance. *Journal of Turbomachinery*. 142 (8): 081007. https://doi.org/10.1115/1.4046528.

Cappiello A. and Tuccillo R. (2021a). Design parameter influence on losses and downstream flow field uniformity in supersonic ORC radial-inflow turbine stators. *International Journal of Turbomachinery, Propulsion and Power*. 6 (3). https://doi.org/10.3390/ijtpp6030038.

Cappiello A. and Tuccillo R. (2021b). Influence of supersonic nozzle design parameters on the unsteady stator-rotor interaction in radial-inflow turbines for organic Rankine cycles. In Turbo Expo: Power for Land, Sea, and Air.

Cappiello A., Majer M., Tuccillo R., and Pini M. (2022). On the influence of stator-rotor radial gap size on the fluid-dynamic performance of mini-ORC supersonic turbines. In Turbo Expo: Power for Land, Sea, and Air, Vol. 10B.

Chen H., and Baines N. C. (1994). The aerodynamic loading of radial and mixed-flow turbines. *International Journal of Mechanical Sciences*. 36 (1): 63–79. https://doi.org/10.1016/0020-7403(94)90007-8.

Colonna P., Casati E., Trapp C., Mathijssen T., Larjola J., et al. (2015). Organic Rankine cycle power systems: From the concept to current technology, applications, and an outlook to the future. *Journal of Engineering for Gas Turbines and Power*. 137 (10): 100801. https://doi.org/10.1115/1.4029884.

Coull J. D. (2017). Endwall loss in turbine cascades. *Journal of Turbomachinery*. 139 (8): 081004. https://doi.org/10.1115/1.4035663.

Da Lio L. (2019). Preliminary design of organic fluid turbines to predict the efficiency. PhD thesis, University of Padova.

De Servi C. M., Burigana M., Pini M., and Colonna P. (2019). Design method and performance prediction for radial-inflow turbines of high-temperature mini-organic Rankine cycle power systems. *Journal of Engineering for Gas Turbines and Power*. 141 (9): 091021. https://doi.org/10.1115/1.4043973.

Denton J. D. (1993). Loss mechanisms in turbomachines. *Journal of Turbomachinery*. 115 (4): 621–656. https://doi.org/10.1115/1.2929299.

Dhillon A. K. and Ghosh P. (2021). Exergetic analysis of reverse Brayton cryocooler with different turbine arrangements for HTS power cables. *Cryogenics*. 115: 103262. https://doi.org/10.1016/j.cryogenics.2021.103262.

Giles M. B. (1988). Calculation of unsteady wake/rotor interaction. *Journal of Propulsion and Power*. 4 (4): 356–362. https://doi.org/10.2514/3.23074.

Giuffre' A., and Pini M. (2021). Design guidelines for axial turbines operating with non-ideal compressible flows. *Journal of Engineering for Gas Turbines and Power*. 143 (1): 011004. https://doi.org/10.1115/1.4049137.

Glassman A. J. (1976). Computer program for design analysis of radial-inflow turbines, Technical report d-8164, NASA.

Guardone A., Colonna P., Pini M., and Spinelli A. (2024). Nonideal compressible fluid dynamics of dense vapors and supercritical fluids. *Annual Review of Fluid Mechanics*. 56: 241–269. https://doi.org/10.1146/annurev-fluid-120720-033342.

Harinck J., Guardone A., and Colonna P. (2009). The influence of molecular complexity on expanding flows of ideal and dense gases. *Physics of Fluids*. 21 (8): 086101. https://doi.org/10.1063/1.3194308.

Huber M. L., Lemmon E. W., Bell I., and McLinden M. O. (2022). The NIST REFPROP database for highly accurate properties of industrially important fluids.

Jones A. C. (1996). Design and test of a small, high pressure ratio radial turbine. *Journal of Turbomachinery*. 118 (2): 362–370. https://doi.org/10.1115/1.2836651.

Kouremenos D. A., and Kakatsios X. K. (1985). The three isentropic exponents of dry steam. *Forschung im Ingenieurwesen*. 51 (4): 117–122. https://doi.org/10.1007/BF02558416.

Krempus D., Beltrame F., Majer M., Servi C. M. D., Vos R., and Colonna P. (2023). ORC waste heat recovery system for the turboshaft engines of turboelectric aircraft. In Aerospace Europe Conference 2023.

Leto A., and Bonfiglioli A. (2017). Preliminary design of a radial turbine for methane expander rocket-engine. *Energy Procedia*. 126: 738–745. https://doi.org/10.1016/j.egypro.2017.08.221.

Mack Y., Haftka R., Griffin L., Snellgrove L., Dorney D., Huber F., and Shyy W. (2006). Radial turbine preliminary aerodynamic design optimization for expander cycle liquid rocket engine. In 42nd AIAA/ASME/SAE/ASEE Joint Propulsion Conference Exhibit'.

Manfredi M., Alberio M., Astolfi M., and Spinelli A. (2021). A reduced-order model for the preliminary design of small-scale radial inflow turbines. In Vol. 4 of Turbo Expo: Power for Land, Sea, and Air.

Manfredi M., Spinelli A., and Astolfi M. (2023). Definition of a general performance map for single stage radial inflow turbines and analysis of the impact of expander performance on the optimal ORC design in on-board waste heat recovery applications. *Applied Thermal Engineering*. 224: 119857. https://doi.org/10.1016/j.applthermaleng.2022.119857.

Matabuena L. S. (2023). Radial turbine-diffuser interaction: effect of tip gap. Master's thesis, Delft University of Technology.

Meitner P. L. and Glassman A. J. (1983). Computer code for off-design performance analysis of radial-lnflow turbines with rotor blade sweep. In Technical Report 83-c-4, NASA.

Mounier V., Olmedo L. E., and Schiffmann J. (2018). Small scale radial inflow turbine performance and pre-design maps for organic Rankine cycles. *Energy*. 143: 1072–1084. https://doi.org/10.1016/j.energy.2017.11.002.

Najjar Y. S. and Radhwan A. M. (1988). Cogeneration by combining gas turbine engine with organic Rankine cycle. *Heat Recovery Systems and CHP*. 8: 211–219. https://doi.org/10.1016/0890-4332(88)90057-9.

Nosaka M., Takada S., Kikuchi M., Sudo T., and Yoshida M. (2004). Ultra-high-speed performance of ball bearings and annular seals in liquid hydrogen at up to 3 million DN (120,000 rpm). *Tribology Transactions*. 47: 43–53. https://doi.org/10.1080/05698190490279047.

Perdichizzi A. and Lozza G. (1987). Design criteria and efficiency prediction for radial inflow turbines. In Vol. 1 of Turbo Expo: Power for Land, Sea, and Air.

Roache P. J. (1998). Verification and validation in computational science and engineering. Hermosa Publishers, Albuquerque, New Mexico.

Rodgers C. (1987). Performance of a high-efficiency radial/axial turbine. *Journal of Turbomachinery*. 109 (2): 151–154. https://doi.org/10.1115/1.3262077.

Sauret E. (2012). Open design of high pressure ratio radial-inflow turbine for academic validation. In Vol. 7 of ASME International Mechanical Engineering Congress and Exposition. pp. 3183–3197.

Sieverding C. H., Stanislas M., and Snoeck J. (1980). The base pressure problem in transonic turbine cascades. *Journal of Engineering for Power*. 102 (3): 711–718. https://doi.org/10.1115/1.3230330.

Span R., and Wagner W. (1996). A new equation of state for carbon dioxide covering the fluid region from the triple-point temperature to 1100 K at pressures up to 800 MPa. *Journal of Physical and Chemical Reference Data*. 25: 1509–1596. https://doi.org/10.1063/1.555991.

Swift W., Zagarola M., Nellis G., McCormick J., Sixsmith H., and Gibbon J. (1999). Developments in turbo Brayton technology for low temperature applications. *Cryogenics*. 39: 989–995. https://doi.org/10.1016/S0011-2275(99)00117-4.

Symes R., Djaname T.-N., Deligant M., and Sauret E. (2021). Design and optimization of a radial inflow turbine for use with a low temperature ORC. *Energies*. 14 (24). https://doi.org/10.3390/en14248526.

Tosto F. (2023). Modeling and characterization of non-ideal compressible flows in unconventional turbines. PhD thesis, Delft University of Technology.

Tosto F., Giuffré A., Colonna P., and Pini M. (2022). Flow deviation and critical choking in transonic turbine cascades operating with non-ideal compressible flows. *Journal of the Global Power and Propulsion Society*. 6: 181–199. https://doi.org/10.33737/jgpps/151659.

Tosto F., Wheeler A., and Pini M. (2024). Investigation of non-ideal effects in compressible boundary layers of dense vapors through direct numerical simulations. *Physics of Fluids*. 36 (1): 016145. https://doi.org/10.1063/5.0179570.

Vimercati D., Gori G., and Guardone A. (2018). Non-ideal oblique shock waves. *Journal of Fluid Mechanics*. 847: 266–285. https://doi.org/10.1017/jfm.2018.328.

Whitfield A. and Baines N. C. (1990). Design of radial turbomachines. Pearson Education, Harlow, Essex, England and New York, NY.

Wittmann T., Lück S., Bode C., and Friedrichs J. (2021a). Modelling the condensation phenomena within the radial turbine of a fuel cell turbocharger. *International Journal of Turbomachinery, Propulsion and Power*. 6 (3). https://doi.org/10.3390/ijtpp6030023.

Wittmann T., Lück S., Hertwig T., Bode C., and Friedrichs J. (2021b). The influence of condensation on the performance map of a fuel cell turbocharger turbine. In Vol. 6 of Turbo Expo: Power for Land, Sea, and Air.

Wittmann T., Lück S., Friedrichs J., Wiśniewski P., and Dykas S. (2022). Analysis of the condensation phenomena within the radial turbine of a fuel cell turbocharger. In Vol. 10B of Turbo Expo: Power for Land, Sea, and Air.